



Effect of Strain Rate on Mechanical Behavior and Microstructure Evolution of Ti-Based T110 Alloy

Pavlo E. Markovsky¹ · Jacek Janiszewski² · Vadim I. Bondarchuk¹ · Oleksandr O. Stasyuk¹ · Kamil Cieplak² · Olga P. Karasevska^{1,3}

Received: 12 August 2021 / Revised: 18 October 2021 / Accepted: 19 October 2021 / Published online: 8 December 2021
© ASM International 2021

Abstract

Recently developed thermally hardenable medium-level alloyed titanium alloy T110 was studied from the viewpoint of microstructure influence on the mechanical behavior under quasi-static and high-strain rate deformation. The globular microstructures of two types differing in aspect ratio of α -globules were formed under thermomechanical processing conditions with different reductions ($\epsilon_{\text{total}} = 2$, and 3) and final annealing at 850 °C, 3 h. The thermally hardened state was formed by conventional solid-solution treatment at a temperature of two-phase $\alpha+\beta$ field (880 °C, 45 min), water quenching, and final aging (550 °C, 5 h). Stress–strain dependencies were estimated on tension with strain rates varied from $8 \cdot 10^{-4}$ to $4 \cdot 10^{-2} \text{ s}^{-1}$, as well as compression with a strain rate of 10^{-3} s^{-1} (quasi-static) and under high-strain rates varied from 870 s^{-1} to 3520 s^{-1} ; the deformation with high-strain rates has been achieved using split Hopkinson pressure bar (SHPB) technique. The tested material was also assessed using strain energy (SE) parameter. A parallel study of the microstructure and crystallographic texture formed during testing allowed to propose a reliable deformation and fracture mechanisms, depending on the stress state (tension, compression) and strain rate. A special role of the initial microstructure is noted, which determines the plasticity of the tested alloy, the sites of pore nucleation, features of crack growth, as well as the localization of deformation, which is determined by the mode and rate of loading. It is established and explained why the best balance of strength and ductility, and thus, the highest SE values in the all tests carried out were ensured by the alloy in the state with a more uniform microstructure of globular morphology (after the rolling with reduction $\epsilon_{\text{total}} = 3$), which, in turn, provided general superiority over the widely used Ti-6Al-4V alloy.

Keywords Titanium alloy · Microstructure · Mechanical properties · Tension · Quasi-static compression · High-strain rate compression · Split Hopkinson pressure bar

Abbreviations

| | |
|--------|--|
| Ti64 | Commercial titanium alloy containing 6 (wt.%) Al and 4 % V |
| Ti64GL | Ti64 alloy with globular microstructure |
| T110 | Titanium alloy with nominal composition |

| | |
|---------------------------------|--|
| $\alpha, \alpha_I, \alpha_{II}$ | H.c.p. alpha phase in the initial state; remnants of primary alpha phase, and secondary alpha phase formed on different treatments, respectively |
| β | B.c.c. beta phase |
| α' | Alpha prime martensite |
| AN | Annealed state of T110 alloy after annealing at 850 °C, 3 h |
| STA | Solution treated and aged state after corresponding strengthening heat treatment |
| FH | Furnace heating |
| FC | Furnace cooling |
| AC | Air cooling |
| WQ | Water quenching |
| XRD | X-ray Diffraction |
| SE | Strain energy |
| QSC | Quasi-static compression |

✉ Pavlo E. Markovsky
pmark@imp.kiev.ua

¹ G.V. Kurdyumov Institute for Metal Physics of N.A.S. of Ukraine, 36, Academician Vernadsky Boulevard, Kyiv 03142, Ukraine

² Jarosław Dąbrowski Military University of Technology, 2, gen. Sylwester Kaliski str., 00-908 Warsaw 46, Poland

³ National Technical University of Ukraine “Igor Sikorsky Kyiv Polytechnic Institute”, 37, Peremohy Ave, Kyiv 03056, Ukraine

| | |
|-------------------------------|--|
| SHPB | Split Hopkinson pressure bar (testing method, apparatus) |
| OM | Optical microscopy |
| SEM | Scanning electron microscopy |
| SEI | Secondary electrons (image) |
| BSE | Backscattered electrons (image) |
| EBSD | Electron backscattering diffraction |
| OIM | Orientation image map |
| BF TEM | Bright field transmission electron microscopy |
| ASB | Adiabatic shear band |
| RD | Rolling direction of T110 plates in pole figures and for cutting out specimens for compression tests |
| TD | Transverse direction of T110 plates in pole figures and for cutting out specimens for compression tests |
| ϵ_{total} | Total reduction on rolling |
| $\dot{\epsilon}_{\text{max}}$ | Maximal strain rate at which specimens did not fracture during SHPB tests |
| $\dot{\epsilon}_{\text{Cr}}$ | Critical (minimal) strain rate at which specimens started to fracture during high-strain rate SHPB tests |
| SE_{max} | Maximal strain energy value obtained on SHPB impact tests at maximal strain rate |
| YS | Yield strength (on tension) |
| UTS | Ultimate tensile strength (on tension) |
| El | Relative elongation (on tension) |
| RA | Reduction in area (on tension) |

Introduction

Titanium alloys are one of most important structural materials employed for different applications due to the unique combination of high specific strength, fracture toughness, crack propagation resistance, creep, corrosion resistance, and non-magnetism [1–3]. Since these alloys are more and more widely used in critical products of aerospace and military technologies, higher requirements are being put forward to their physical, mechanical, and service properties [4, 5]. In order to improve the balance of service properties or some specific characteristics, continuous work is carried out on both obtaining new compositions of titanium-based alloys and developing advanced methods for their production and treatment [5, 6]. In particular, titanium alloy T110 (Ti-Al-V-Mo-Fe-Zr-Nb system) was designed as a new weldable and hardenable material. Heat treatments of this alloy in the two-phase $\alpha+\beta$ field allow to achieve strength above 1100 MPa in welded joints. Besides, a good balance of various mechanical properties of the alloy can be obtained after a number of processing routes, which can be employed for critical products, including aerospace and military applications [6–8]. For instance, ballistic testing of T110 sheets

with the use of various type of live ammunition showed at least 20–25% higher ballistic resistance compared to the commonly used for this purpose Ti-6Al-4V alloy [6, 9, 10]. However, the dependence of the mechanical properties of the T110 alloy on the various types of processing and the structure-phase state created by them has been studied to a very limited extent, mainly by standard tensile tests. There is practically no information on the mechanical behavior of the T110 alloy under various stress modes and strain rates. Therefore, the present work is devoted to the study of the effect of the stress mode (tension or compression) and the loading condition (quasi-static and high-strain rate) on the mechanical behavior of the T110 alloy stabilized by annealing, as well as after standard (furnace heating followed by quenching and final aging) strengthening heat treatment.

Materials and Experimental Procedure

The T110 alloy with actual composition Ti-3.9(wt.%) Al-0.8V-1.5Mo-2.1Fe-0.7Zr-3.8Nb was melted in Scientific & Production Centre “Titan” (Kyiv, Ukraine [11, 12]) using double-melting Electron Beam Cold Hearth method; cylindrical ingot with diameter 110 mm and length 200 mm was produced. The ingot was stripped and then subjected to multi-step thermomechanical processing followed by heat treatments (Fig. 1a). Thermomechanical treatment includes: firstly, 3D pressing with total reduction not less than 70% at temperature above beta-transus temperature (T_{β} —the temperature of $\alpha+\beta_0 \rightarrow \beta$ polymorphous transformation completing under equilibrium conditions of furnace heating [1, 2]), and then cross-rolling at temperature about 50 °C below T_{β} .¹ This rather conventional processing was described in more details in.[5, 9] To study the effect of the degree of the microstructure transformation (formation of as more as possible homogeneous microstructure of globular type with aspect ratio close to 1), the final cross-rolling of pressed semi-product was carried out with different reductions of plate thickness (h) to 15 mm ($\epsilon_{\text{total}} = 2$, including 3D pressing stage, Fig. 1a), and 10 mm ($\epsilon_{\text{total}} = 3$). After hot deformation, heat treatment (annealing at 850 °C, 3 h, slow cooling with furnace) was applied to stabilize phase composition and microstructure. To assess the effect of heat hardening on the mechanical behavior in various stress modes, some specimens after the rolling with $\epsilon_{\text{total}} = 2$ were subjected to the following heat treatment: solid solutioning at 880 °C, 45 min, water quenching, and final aging at 550 °C, 5 h.

The mechanical properties of the T110 alloy in all microstructural states mentioned above were determined in tensile and compression tests. Tensile tests were performed on

¹ For the above mentioned actual composition $T_{\beta} = 910$ °C.

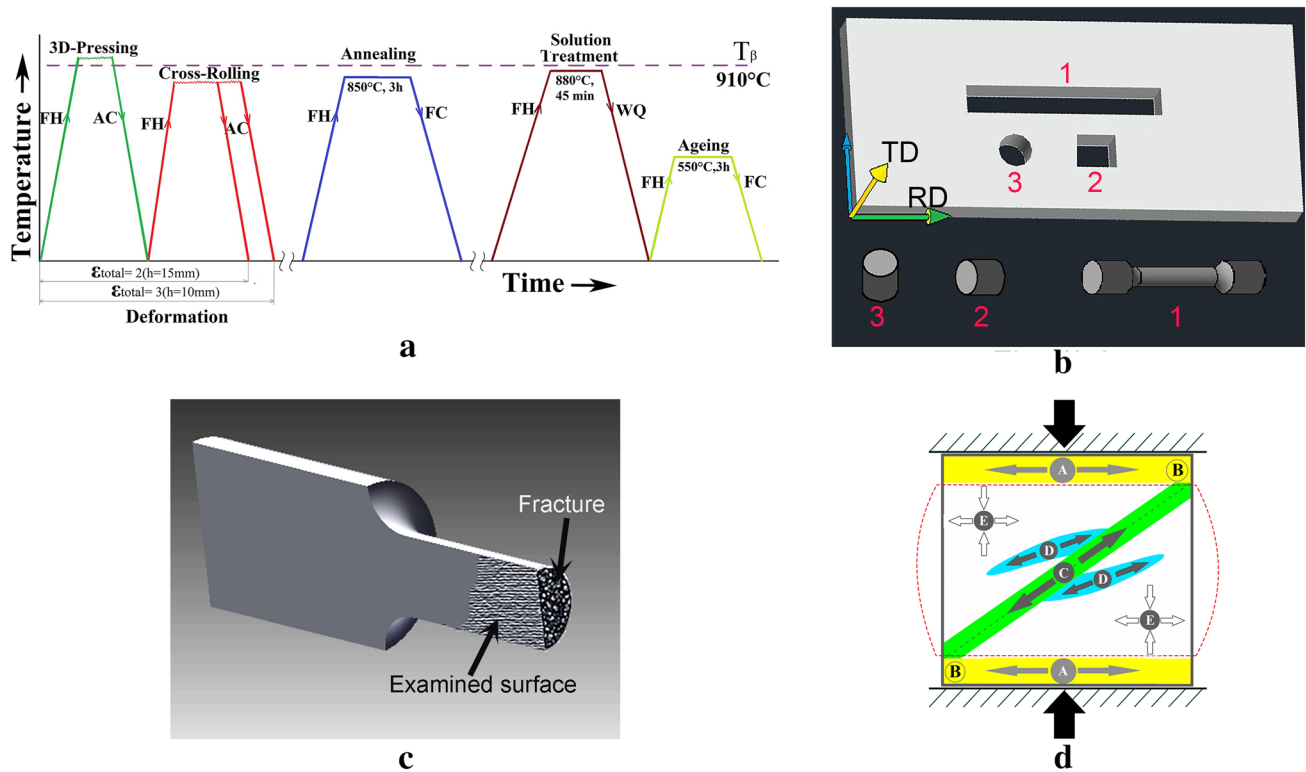


Fig. 1. Schemes of: (a) thermomechanical and heat treatments employed for the T110 ingot processing; (b) cutting out of rolled plates test specimens for: (1) tension in RD, and compression in (2) RD and (3) TD; (c) sample sectioning for SEM and TEM stud-

ies of fractured zone after tensile tests; (d) representation of specific zones distinguished in the longitudinal section of compression tested cylindrical specimens: the capital letters indicate the locations where microstructure was studied in detail.

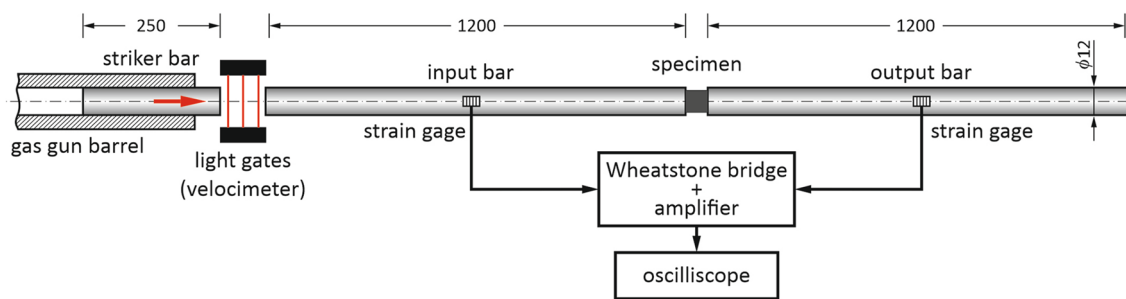


Fig. 2. The scheme of the split Hopkinson pressure bar (SHPB) system used in the study.

cylindrical specimens with gage diameter 4 mm and length 25 mm (cut out of the plate as shown in Fig. 1b, #1) using an INSTRON 3376 machine according to ASTM E8 standard. Tension rates were varied from $8 \cdot 10^{-4} \text{ s}^{-1}$ to $3.6 \cdot 10^{-2} \text{ s}^{-1}$. In turn, quasi-static and high-strain rate compression tests were conducted on cylindrical specimens of 5 mm diameter and 5 mm length, which were cut of the plate in rolling (RD) and transverse (TD) directions as shown in Fig. 1b, #2 and #3, respectively. The high-strain rate compression tests were performed by means of the classical split Hopkinson pressure bar (SHPB) technique [13–15] using the

system schematically shown in Fig. 2. The compression rate was 10^{-3} s^{-1} for the QSC tests, whereas for the SHPB experiments varied from 870 s^{-1} to 3520 s^{-1} . More details on the applied SHPB setup are given in our previous work [16]. The structure of all materials was studied with optical microscopy (OM) at an XL70 (Olympus, Japan) and scanning electron microscopy (SEM) at VEGA3 and MIRA3 microscopes (both TESCAN, Czech Republic). The microstructure of tensile tested specimens was also analyzed on sections cut perpendicular to the fracture surface in longitudinal direction of the specimens close to the fracture

site (Fig. 1c). The microstructure of compression tested specimens was studied on samples cut and polished in longitudinal direction [16]. The maps of local orientations of some specimens in different states were obtained by electron backscatter diffraction (EBSD) technique at SEM MIRA3. The phase composition and crystallographic texture were examined by x-ray diffraction analysis at an ULTIMA IV (RIGAKU, Japan) diffractometer. Fine substructure was investigated with transmission electron microscopy (TEM) at a JEM-2000FXII microscope (JEOL, Japan) at accelerating voltage of 200 kV. The foils for TEM studies (3 mm in diameter) were prepared by double-jet electro-polishing in the electrolyte consisting of 60% methanol, 35% butanol, and 5% perchloric acid at -40 °C. Metallographic specimens for OM, SEM, and EBSD study after standard grinding and polishing were prepared using Saphir Vibro polishing machine (ATM, Germany).

Results

Initial Microstructure, Phase Composition, and Crystallographic Texture

As for all titanium two-phase $\alpha+\beta$ alloys [5], the microstructure of the T110 alloy is mainly determined by the deformation-force and temperature conditions of thermomechanical treatment. The basics of the influence of the thermomechanical treatment mode on the evolution of the T110 microstructure were considered in [9]. The thermomechanical treatment regimes used in this study in combination with the subsequent annealing allowed to transform the initial coarse-grained lamellar structure (Fig. 3a) into an almost fully globular one (Fig. 3b, c, h). The higher deformation ($\epsilon_{\text{total}} = 3$) ensured the formation of more uniform and perfect globular microstructure in comparison with the lower one ($\epsilon_{\text{total}} = 2$) (compare Fig. 3h with 3b, c). After the lower deformation, the microstructure of the T110 alloy had not completely transformed (recrystallized) morphology of phase constituents, and the majority of α -lamellas were elongated in rolling direction (Fig. 3b, c). It should be also noted that the employed thermomechanical processing and subsequent cooling led to appearance of small amount of rather fine secondary α_{II} -lamellae, which did not disappear even upon final annealing (Fig. 3c). The differences in the degree of applied deformation and the completeness of the transformation from lamellar to globular microstructure are also accompanied by changes in the intensity of x-ray peaks (Fig. 4a, b) and in crystallographic texture of the samples (Fig. 4c–f). The presence of all possible reflections of both α - and β -phases in the specimens cut out of 15 mm and 10 mm thick plates (Fig. 4a, b, respectively) indicates the absence of too sharp crystallographic textures in them.

Nevertheless, a comparison of the intensities of reflections for 15 mm and 10 mm thick plates allows to reveal some essential difference in their texture conditions, which is confirmed by the features of the pole figures (Fig. 4c–f). The comparison clearly shows that the higher degree of plastic deformation (10 mm thick plate) applied by rolling in the two-phase $\alpha + \beta$ field has led to the formation of more sharp and pronounced textures for both basal (002) planes in the α -phase and (200) planes of β -phase (Fig. 4d, f versus c and e, respectively).

Application of STA strengthening heat treatment at the temperatures of two-phase $\alpha+\beta$ field, commonly used for titanium alloys with similar content of alloying elements [1, 17], caused decrease in the number and size of the particles of primary α -phase after solid-solution treatment and quenching (Fig. 3d). The final microstructure after aging is sometimes named as “heterogeneous” because it consists of abovementioned remnants of primary α -phase (denoted as α_{I} in Fig. 3e–g) and fine secondary α_{II} -particles which precipitated inside the β -phase matrix during isothermal exposure at aging temperature (Fig. 3e–g). Exactly this finer $\alpha_{\text{II}}+\beta$ mixture provides the hardening effect [1]. Since the high-temperature stage of heat-strengthening treatment was carried out in the two-phase $\alpha + \beta$ field (i.e., the $\alpha + \beta \rightarrow \beta \rightarrow \alpha'(\alpha'')$, phase transformation was uncompleted, that ensured remnants of primary α_{I} -particles), the crystallographic texture of the material remained practically unchanged.

Quasi-static Mechanical Properties

Tension Testing

Typical examples of tensile curves (the specimens for testing were cut out in rolling direction (RD)) are presented in Fig. 5. In both as-annealed conditions, the alloy had yield strength of about 1000 MPa and high ductility—true strain reached 0.15 and 0.18 for 15 mm and 10 mm thick plate, respectively, although yield stress at strain rates $8 \cdot 10^{-4} \text{ s}^{-1}$ was slightly lower than at $3.6 \cdot 10^{-2} \text{ s}^{-1}$ (Fig. 5a, c). STA hardening caused essential increase in yield strength—up to 1500 MPa (Fig. 5b), while true strain dropped by about half. The increase in the tension rate for all structural states was accompanied mainly by a noticeable decrease in ductility, while the strength remained practically unchanged. If we compare these characteristics with the Ti-6-4 alloy tested in a similar way [1, 18, 19], it should be noted that the T110 alloy has noticeably higher strength, especially after STA hardening. This superiority in strength is associated with higher content of β -stabilizing alloying elements and, hence, higher volume fraction of the β -phase which contributes into strengthening processes during STA hardening heat treatment as compared to less alloyed Ti-6-4 alloy. Comparing 10 mm and 15 mm thick plates, it should

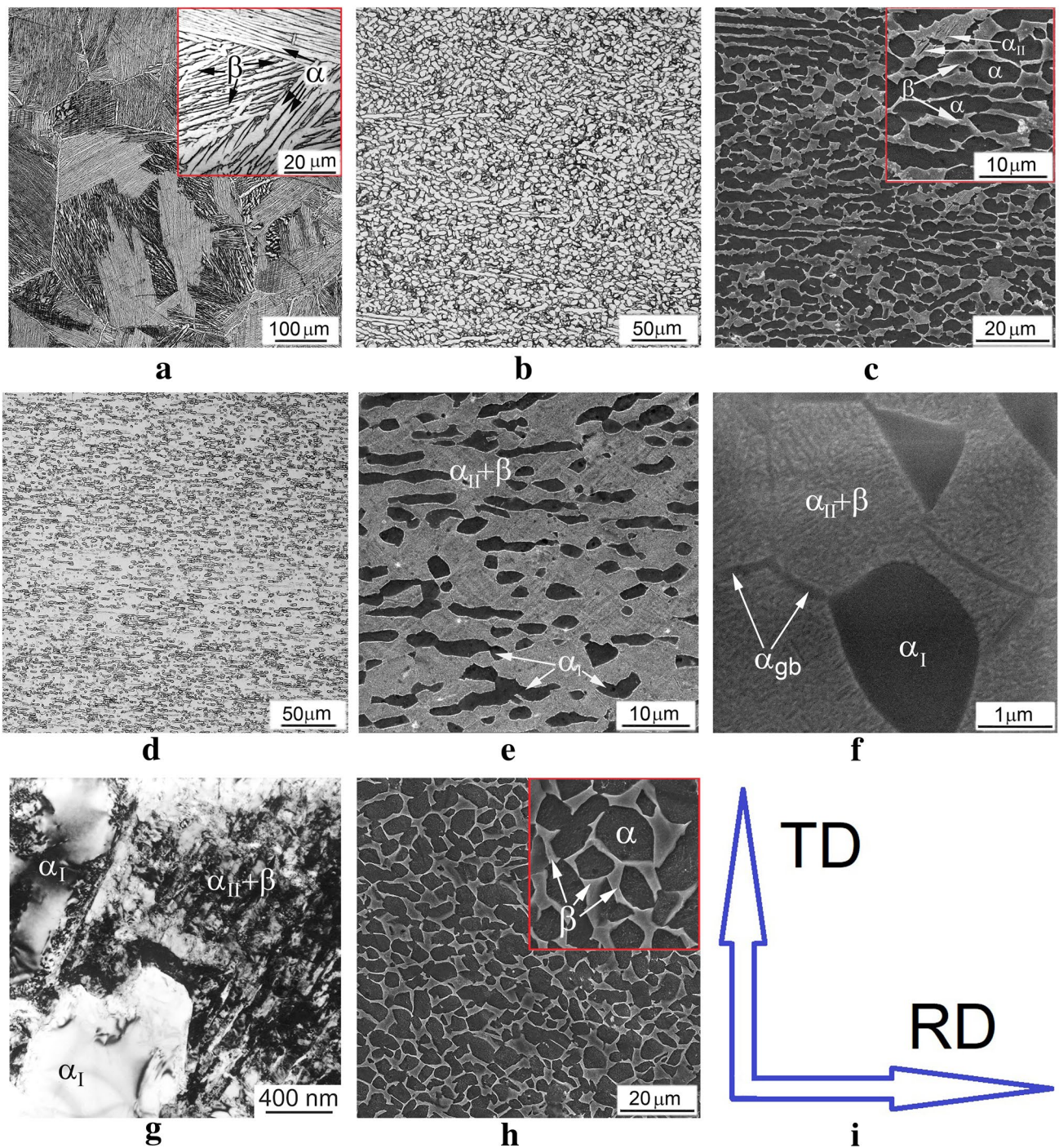


Fig. 3. Microstructure of the T110 alloy in (a) as-cast and (b-h) deformed conditions. Plates (b–g) 15 mm thick, (h) 10 mm thick, at heat treatment conditions: (b, c, h) annealed (850 °C, 3 h, furnace cooling (FC)), (d–g) STA (880 °C, 45 min, water quenched (WQ),

and then aged 550 °C, 5 h). (a, b, d) OM, (c, e, h) SEM, SEL; (f) SEM, BSE, (g) TEM. (i) Designation of RD and TD directions on microstructures (b–f, h).

be noted that the first of them, due to the more homogeneous structure of more equiaxed α -globules, has higher plasticity at the same strain rates (Fig. 5c vs. a), while the strength level is approximately the same because of rather similar size of microstructure constituents, first of

all α -particles (Fig. 3g vs. b). Both materials demonstrate rather low work hardening on tension (Fig. 5a, c); at the same time, STA-hardened specimens did not show visible work hardening effect in tension (Fig. 5b).

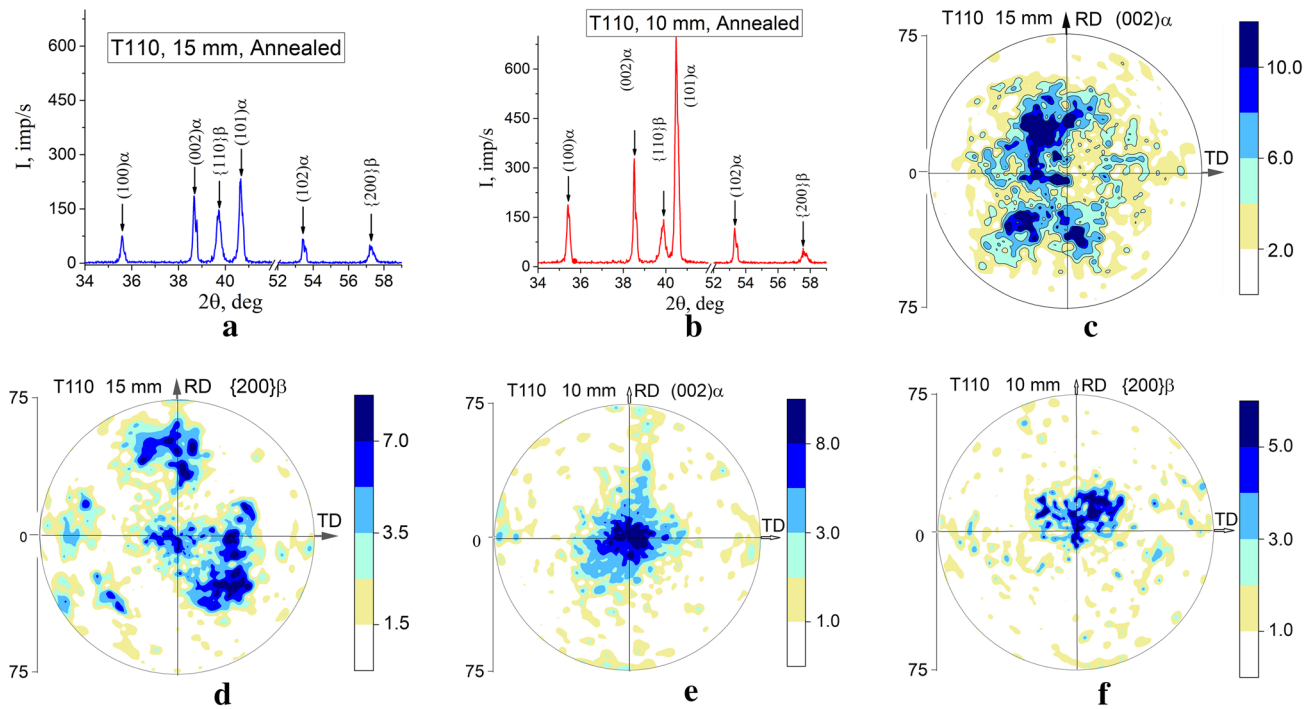


Fig. 4. XRD patterns (**a, b**) and pole figures of (**c, e**) (002) α - and (**d, f**) {200} β -phases of T110 in annealed condition; plate thickness—(**a, c, d**) 15 mm and (**b, e, f**) 10 mm.

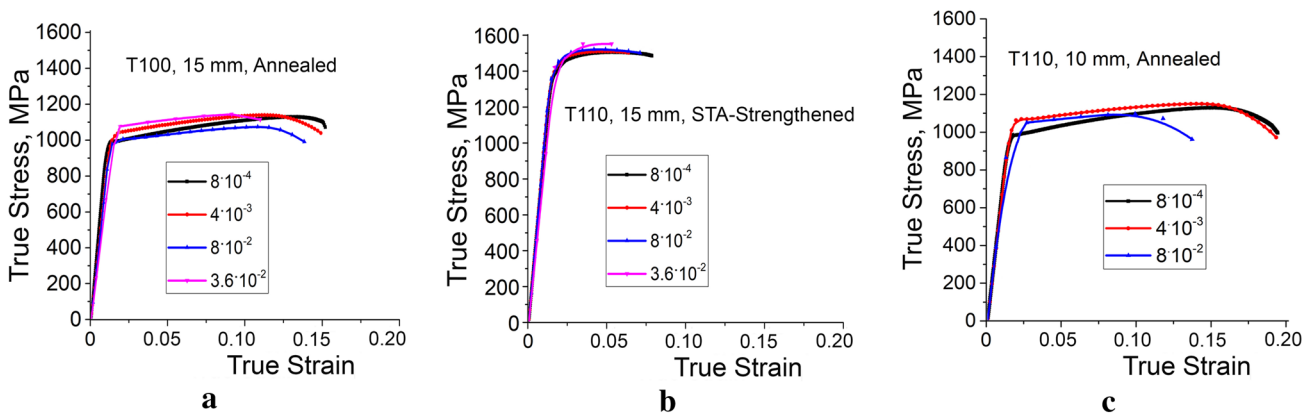


Fig. 5. True stress-strain curves of the T110 alloy tested at quasi-static strain rate regime: (**a, b**) 15 mm thick plate, (**c**) 10 mm thick plate, in (**a**, **c**) annealed and (**b**) STA-hardened conditions. Specimens were cut out, machined, and tested in RD direction.

Compression Testing

The QSC tests (as well as high-strain rate SHPB compression tests) were performed in two parallel directions: along rolling direction (RD) and in transverse direction (TD). The results of QSC tests are shown in Fig. 6. First of all, it is worthwhile to note that the annealed 15 mm thick material showed more than two times higher fracture strain when tested in rolling direction compared with transverse one, despite the fact that both stress-strain curves had rather

similar shapes (Fig. 6a). The T110 alloy in this annealed microstructural state showed an intensive work hardening during compression: plastic flow stress increased from approximately 1000 MPa to 1300 MPa and 1600 MPa for the specimens tested in TD and RD directions, respectively (curves 1 and 2 in Fig. 6a). STA-hardened 15 mm thick material reached such a high strength (above 1600 MPa) already at the stage of elastic deformation, and further increase in strength was moderate (Fig. 6b). It can be explained by comparatively small amount of primary α_1 -phase which

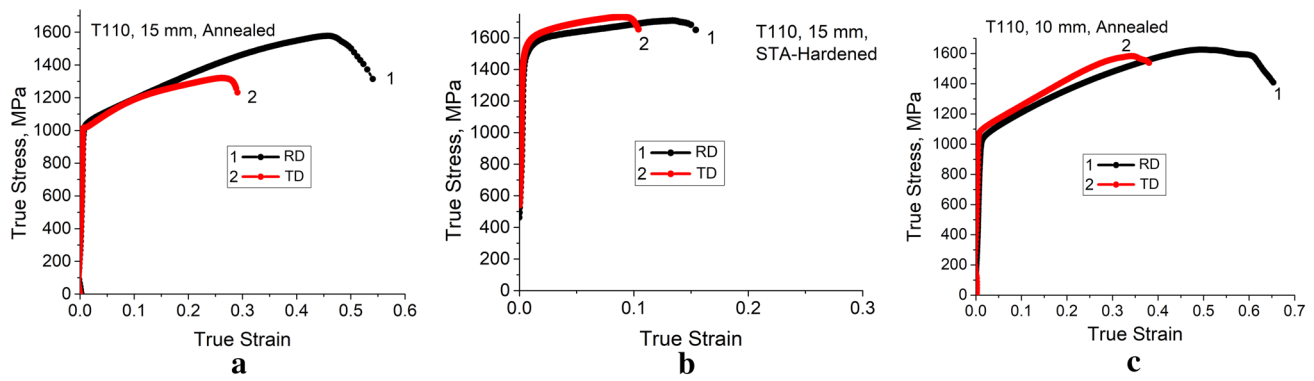


Fig. 6. Quasi-static compression stress-strain curves of (a, b) T110 15 mm thick plate, (c) 10 mm thick plate in (a, c) annealed, and (b) STA-strengthened conditions at strain rate 10^{-3} s^{-1} .

significantly contributes to work hardening during plastic deformation (Fig. 3d–g). Due to the high strength of the $\alpha+\beta$ matrix, strain-hardening capability is greatly reduced—the values of fracture strain are reduced by about three times in comparison with the annealed material state, both for tests in RD and TD direction (Fig. 6b vs. Fig. 6). The mechanical behavior of the specimens cut out from annealed 10 mm thick plate was similar to those cut out from annealed 15 mm thick plate (compare Fig. 6c, a). However, fracture strain values were noticeably higher for both RD and TD directions, whereas the difference in fracture strain values for these two directions was much smaller as compared to annealed thicker plate. The difference in the mechanical properties along RD and TD directions for annealed 15 mm thick plate can be explained by both structural (Fig. 3a, c) and crystallographic (Fig. 4a, b) textures being different in these directions. The specimens made of 10 mm thick plate had more homogeneous microstructure (Fig. 3h) and almost symmetric crystallographic texture (Fig. 4c, d) in both directions; hence, the difference in fracture strain values between RD and TD directions was smaller (Fig. 6c).

High-Strain Rate (SHPB) Compression

Typical examples of stress-strain curves obtained with dynamic compression SHPB tests for all three microstructural types of the T110 alloy for cutting RD and TD directions are shown in Fig. 7. As for most metals [16], high-strain rates cause certain increase in strength and more pronounced decrease in plasticity. Similar to the results of quasi-static compression considered above, high-strain rate tests showed significant difference both between individual structural conditions and between RD and TD cutting directions. For example, the specimens cut out from annealed 15 mm thick plate in RD direction reached a true strain of 0.27 without fracture at a strain rate of 3360 s^{-1} , but it fractured at the strain rate of 3520 s^{-1} (Fig. 7a). In turn, the specimens

cut out in TD direction fractured already at a strain rate of 2570 s^{-1} , and the maximal true strain without fracture was 0.17 only at a strain rate of 2570 s^{-1} (Fig. 7b). The strength level in both RD and TD directions was almost the same and equals approximately 1520 MPa without noticeable strain hardening effect (Fig. 7a, b).

STA hardening of 15 mm thick material caused a noticeable increase in strength (up to almost 2000 MPa) and decrease in fracture strain; however, it was also more pronounced for TD cutting direction (Fig. 7c, d). Maximal true strain achieved in RD direction was equal 0.11 for a strain rate 1520 s^{-1} , whereas at strain rate of 1670 s^{-1} specimen already fractured (Fig. 7c). For TD cutting direction specimens, fracture occurred already at 1230 s^{-1} , and maximal strain was 0.08 only at a strain rate of 1220 s^{-1} (Fig. 7d).

The specimens cut out from annealed 10 mm thick plate showed the best balance of strength and plasticity as compared to other structural states (Fig. 7e, f). For example, the specimens tested in the RD cutting direction showed the maximum strain value of 0.3 at a strain rate of 2810 s^{-1} and did not fracture during the tests (curve 6 in Fig. 7e). For comparison, the specimen cut out from annealed 15 mm thick plate in RD direction had true strain of 0.21 at approximately the same strain rate (2710 s^{-1}), and even at strain rate of 3360 s^{-1} true strain of specimen was only 0.27 (Fig. 7a, curves 3 and 4, respectively). The specimens cut out from annealed 10 mm thick plate in TD direction fractured at a strain rate of 2410 s^{-1} , whereas at 2200 s^{-1} material was still ductile, and it reached maximum strain of 0.24 that is much higher than maximum strain of the specimens cut out from annealed 15 mm thick plate in RD cutting direction (compare curve 6 in Fig. 7f with curve 2 in Fig. 7a). Thus, the annealed specimens cut of a 10 mm thick plate not only had a better balance of strength and ductility than the similar ones cut of a 15 mm plate, but also noticeably less difference in ductility between specimens tested in mutually perpendicular TD and RD directions. The latter fact is clearly

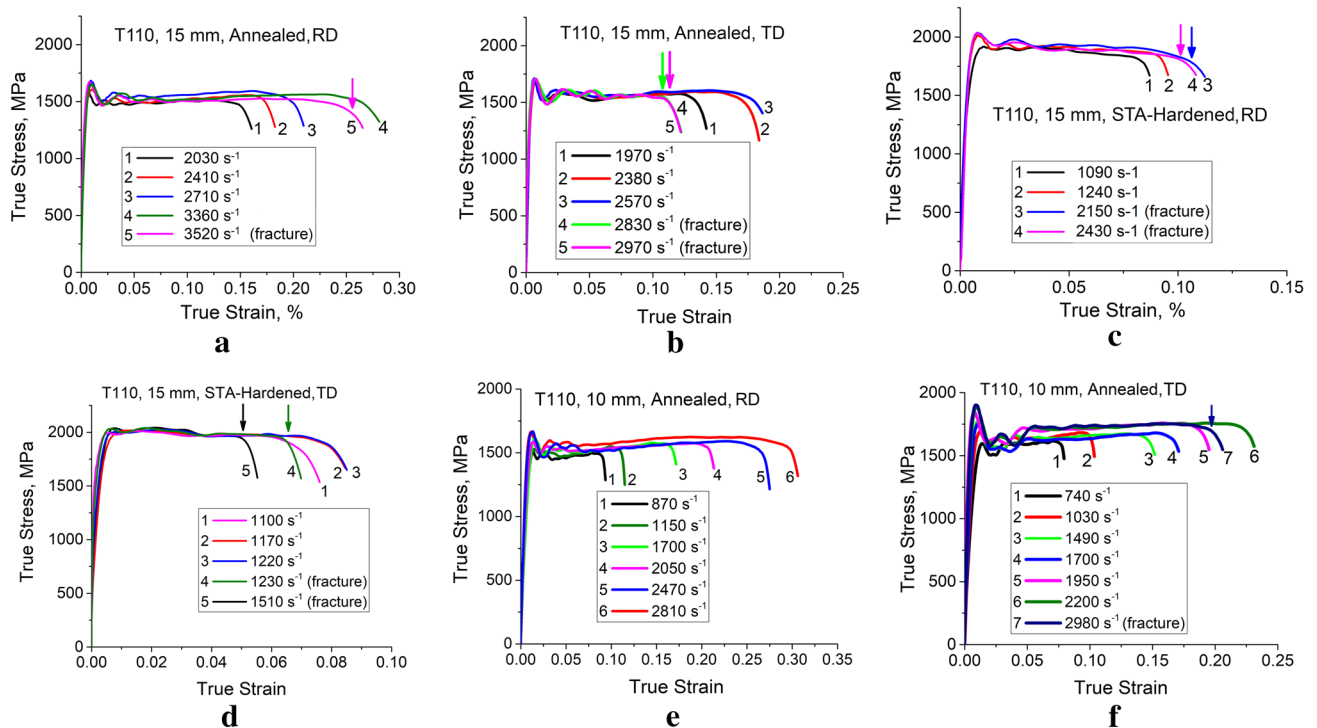


Fig. 7. True stress-true strain SHPB curves of the T110 alloy specimens cut out from (a–d) 15 mm thick plate, and (e, f) 10 mm thick plate in (a, b, e) annealed, and (c, d) STA-hardened conditions tested

in directions (a, c, e) (RD), and (b, d) (TD) directions. Arrows above the curves of corresponding color indicate the specimen cracking.

related to the differences in the crystallographic texture of these plates (see Fig. 4).

Discussion

Strain Energy

As shown earlier [16, 18, 19], strain energy parameter allows to analyze an influence of the strain rate effect on the stress-strain response, taking into account influences of chemical and phase compositions, as well as microstructure of the samples before and after tests. The T110 alloy has sufficient plasticity properties, especially when the phase composition and microstructure are stabilized by annealing. Therefore, values of SE parameters obtained from tensile tests are comparatively high for annealed material state, especially for the samples cut out from the 10 mm thick plate. They exceed even the best values for Ti64GL at strain rates $8 \cdot 10^{-4}$ – $8 \cdot 10^{-2}$ s^{-1} (Fig. 8a). Under quasi-static compression, the advantage of the T110 alloy in the annealed state over Ti64GL material becomes more visible (Fig. 8b) for both RD and TD cutting direction. It should also be noted that the scatter in the SE values measured in QSC tests for TD cutting direction was noticeably larger as compared to RD one (hatched areas of rectangles in Fig. 8b). Likewise, the scatter in SE values

was visibly lower for the specimens cut out from annealed 10 mm thick plate as compared to those cut out from 15 mm thick plate (Fig. 8b). It can be explained by more uniform size and morphology of the α -phase, as well as by more pronounced crystallographic texture in both RD and TD cutting directions in the 10 mm thick plate.

The results of both types of quasi-static experiments for specimens in the STA-hardened state it showed significantly lower SE values in comparison with both the same T110 alloy in annealed state and Ti64GL alloy. Decrease in SE values is mainly related with decreasing plasticity of the T110 alloy in the STA-strengthened state (Fig. 8a, b). It is also worthwhile to note that in the case of the most homogeneous annealed globular microstructure (the 10 mm thick plate, Fig. 3h), the SE level of the samples with the RD cut direction was almost twice as high as in the case of a similar structural state of the Ti-6Al-4V alloy (compare in Fig. 8b the height of the "10 mm, AN, RD" rectangle with the position of the dotted line).

The most complicated and interesting results were obtained from high-strain rate SHPB experiments (Fig. 8c). First of all, it should be noted that comparing the test results in two mutually perpendicular directions (RD and TD), it is clearly seen that for each structure, the dependences of the SE's on the strain rate are initially almost the same for strain range until fracture occurred. For instance, for the

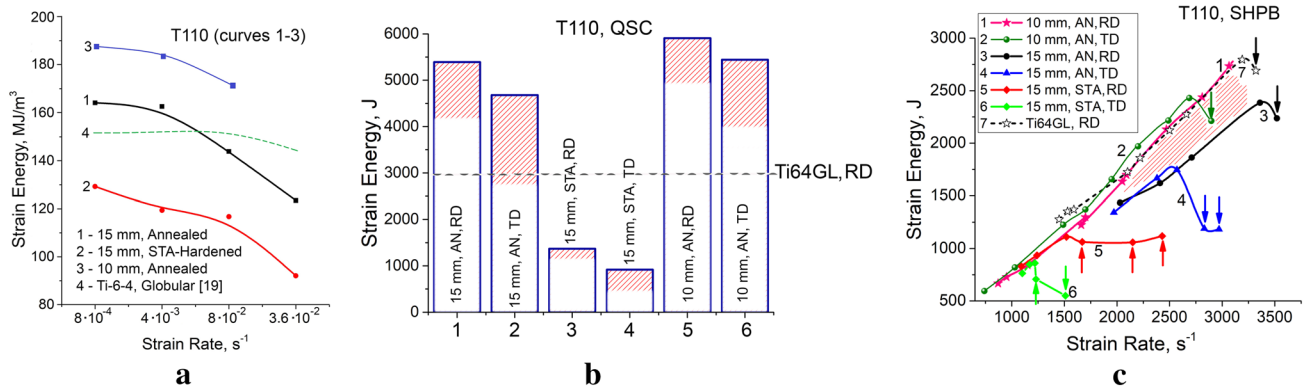


Fig. 8. (Since the numerical results of the SHPB tests are very dependent on a number of characteristics of both the equipment itself and the size of the specimens, SE was calculated as “pure” energy required for the deformation of the specimens with identical size: 5 mm in diameter and 5 mm in height, like in the previous work [16]. Thus, obtained the values directly in Joules, which for dynamic SHPB compression correspond to certain strain rates, and for quasi-static—a certain level of strain. For tension Strain Energy was calculated in MJ/m³.) Strain energy vs. strain rate for (a) quasi-static

tension, (b) quasi-static compression, and (c) high-strain rate SHPB compression. Data for Ti-6-4 alloy with globular microstructure (similar to the T110 alloy—Fig. 1g), curve 4 in (a), horizontal line in (b), and curve 7 in (c), and horizontal line in (b) are adopted from [16, 18]. Hatched areas indicate: (b) the range of strain energy values variation for at least 3 specimens tested, and (c) the SE increase for 10 mm material as compared with 15 mm one. Colored arrows in (c) indicate the specimens of the corresponding states, which fractured on testing.

specimens cut out of the 10 mm thick plate, the SE-strain rate dependencies were parallel to each other for both specimens of the RD and TD cutting directions up to a strain rate of 2910 s⁻¹, at which the TD specimens began to fracture, whereas the RD specimens remained un-cracked throughout the range of strain rates used (compare curves 1 and 2 in Fig. 8c). The same situation is observed in the specimens cut out from annealed 15 mm thick plate tested at 2830 s⁻¹, and in STA-hardened ones tested at 1230 s⁻¹ (curves 3, 4, and 5, 6, respectively, in Fig. 8c). The SE-strain rate curves for the annealed 15 mm thick plate lie much lower than curves of annealed 10 mm thick plate. It is most likely the result of a much lower plasticity of the former material. The difference between the two annealed states (in 10 mm and 15 mm thick plates) is caused mainly by the above-described features of their crystallographic textures (Fig. 4). The STA-hardened specimens when compared to annealed ones are characterized by essentially lower both SE values and strain rates at which fracture occurred (curves 5 and 6 in Fig. 8c). At the initial stage, the behavior of STA-hardened alloy actually coincided with that of the annealed 10 mm thick material, but the former began to crack at much lower strain rates. It can be explained by the fact that, despite of higher strength of strengthened matrix, the cracking initiated at the earlier stages of plastic flow due to comparatively low plasticity.

It is important to note that the best results obtained for the annealed 10 mm thick material tested in the RD cutting direction almost completely coincided with the earlier data [16] obtained from the same tests of the Ti64 alloy with a similar type of globular microstructure (curves 1 and 2 vs. curve 7 in Fig. 8c). This result is somewhat

unexpected because the T110 and Ti64 alloys differ each other in many parameters: namely, chemical composition, the ratio of α- and β-phases, and conventional mechanical characteristics. In addition, they also showed different ballistics resistance against different types of ammunition [6, 9]. Probably, regardless of the above noted differences, both alloys with a well-formed globular microstructure provide such a combination of strength and plasticity under high-strain rate loading that a somewhat lower strength of Ti64GL is compensated by a slightly higher fracture strain. It also should be underlined that the specimens of Ti64GL tested in [16] had almost ideal microstructural state for the cast and wrought Ti64 alloy—they were machined from 10 mm rods and tested in the RD cutting direction that provided optimal mechanical properties for Ti64 alloy.

Fracture and Microstructure Features of Tested Specimens

An analysis of the microstructure of materials after plastic deformation is a primary step to evaluate the difference in their mechanical behavior and deformation mechanisms [16, 18, 19].

Tensile Tests

Figure 9 presents typical examples of fracture surfaces of specimens after tensile tests. First of all, it is worthwhile to note that despite the microstructure has been partially transformed from coarse-grained into near-globular (compare Fig. 3b, c, h with 3a), the delamination (crack opening)

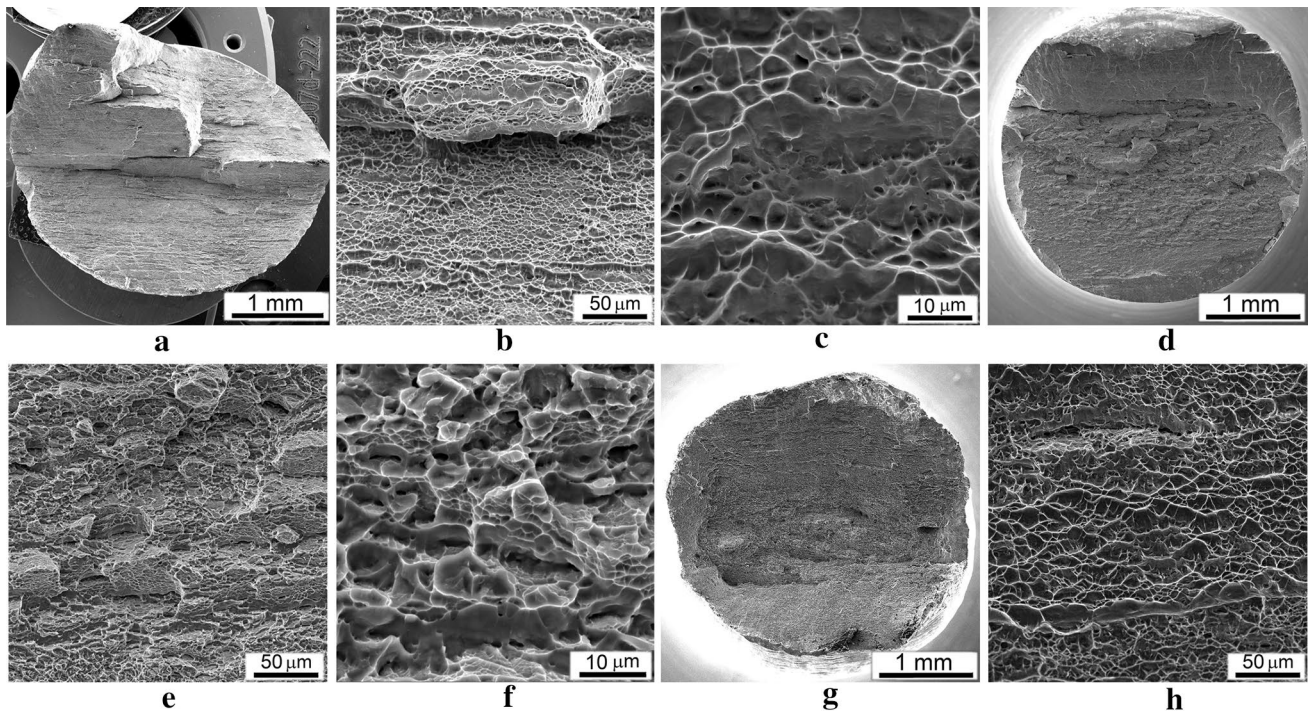


Fig. 9. Fracture surfaces of the tensile tested T110 specimens made of: (a–f) 15 mm, and (g, h) 10 mm thick plates in: (a–c, g, h) annealed, and (d–f) STA-hardened states. SEM, SEL.

between layers formed in annealed specimens by previous rolling² was observed; it was more pronounced in the specimens cut out from the 15 mm thick plate (compare Fig. 9a, d, g). Obviously, this effect related to the structural and crystallographic textures, which were more pronounced in the specimens cut out from the 15 mm thick plate (Figs. 3b, 4a, b). In the STA-hardened condition (Fig. 9d), the strengthened $\alpha_{II} + \beta$ matrix (interlayers of 5–15 μm thickness, Fig. 3e) between primary α_I -phase particles caused comparatively finer fragmentations on the fracture surface (Fig. 9e vs. b). However, at the micro-level the fracture in all three cases (after annealing and after STA hardening) was rather ductile (fine ductile dimples in Fig. 9b, c, e, f, h).

The microstructure close to the fracture surfaces evidences high ductility of the annealed material—there are traces of intense plastic flow in both α - and β -phases in Fig. 10a, b, e, f (compare with the relevant initial states in Fig. 3c, h without traces of plastic deformation). Very few voids indicating the starting stages of crack initiation were observed just under the fracture surface (Fig. 10b, f). Pores formed as a result of a localized shear deformation at an angle of 45° to the applied load direction (Fig. 10a, e). It can

be also noted that in the annealed T110 material, the character of fracture surfaces at the macro- and micro-level was the same both for the specimens cut out from 10 mm thick plate (more uniform and globular microstructure) and from 15 mm thick one (compare Fig. 10e, f with a, b). The α - and β -phases particles near the fracture surface are elongated in the tension direction. Some layers indicated by arrows in Fig. 10e became more stretched in the tension direction than others—they are obviously related to the initial β -grains with specific orientations, which did not completely recrystallize under thermomechanical processing and final annealing. From Fig. 10f, it can be concluded that the size of the smallest dimples (indicated by “A”) clearly corresponds to the size of the initial α -particles (Fig. 3c, h), while the size of coarser dimples (indicated by “B”) can be obviously associated with the size of a cluster of adjacent α -crystals with similar crystallographic orientations (Fig. 10e).

The T110 alloy in the STA-hardened condition contained a slightly more amount of voids in the deeper inside zone of intensive deformation near the fracture surface. Some of these voids formed chains along the line inclined at 45° to the tension direction (Fig. 10c, d). This is obviously explained by much higher strength of the $\alpha_{II} + \beta$ matrix that caused higher localization of stress and plastic deformation as compared to the more ductile annealed material. It is also worthwhile to note that these voids nucleated on the inter-phase boundaries between relatively softer remnants of the

² This affects the mechanical behavior of the material in different ways, when it is tested along other directions, or when other loading patterns are applied (for instance, flexure) [18–21].

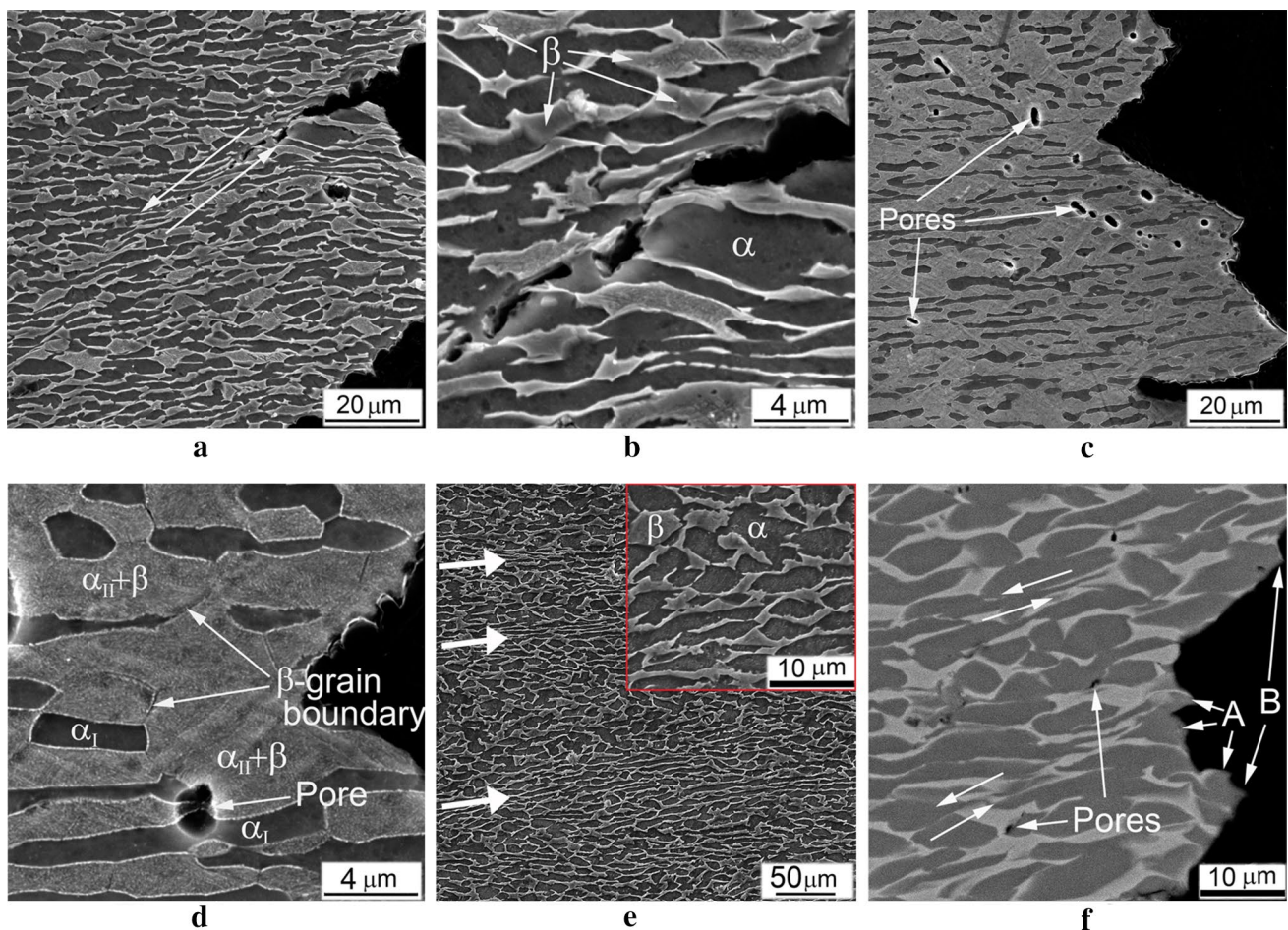


Fig. 10. Microstructure of the T110 alloy (**a–d**) 15 mm and (**e, f**) 10 mm thick plate in locations near the fracture surface after tension with rate $8 \cdot 10^{-2} \text{ s}^{-1}$. (**a, b, e, f**)—annealed (**c, d**)—after STA hardening. Arrows in (**a**) indicate shear line, in (**e**)—most stretched grains,

in (**f**)—shear band. “A” and “B” in (**f**) with relevant arrows indicate the edges of smaller and coarser dimples, respectively. SEM, (**a–e**) SEI, (**f**) BSE.

primary α_I -phase and strengthened $\alpha_{II}+\beta$ -matrix (Fig. 10c, d), that is also typical for the $\alpha+\beta$ titanium alloys strengthened by the same route [1, 22].

The additional information on the features of the deformation mechanisms can be obtained from a comparative study of the changes in the crystallographic micro-texture after plastic deformation.³ Figure 11 shows the results of the EBSD study of an annealed T110 specimen cut out from the 15 mm thick plate in the initial (not deformed) state. As seen from Fig. 11a, b, there are some parallel bands specially oriented along rolling direction. This is most evident for the α -phase (blue, green, and red colored bands in Fig. 11c).

³ The measurements of the macroscopic texture of the alloy after mechanical tests did not show any noticeable changes in comparison with the initial state due to the fact that the XRD method, on the one hand, is integral and covers various zones of specimens (see Fig. 1c, and, on the other hand, provides information for a very thin surface layer only.

These bands with similar crystallographic orientation are clear evidence of incomplete recrystallization of initial as-cast coarse-grained lamellar structure during thermo-mechanical processing [1, 5, 22]. As for the β -phase, it is possible to distinguish small areas that presumably are the remnants of the primary β -grains (the areas of similar colors in Fig. 11d) which mainly underwent the polymorphic $\beta \rightarrow \alpha$ transformation upon cooling. In other words, after rolling and annealing (i.e., after phase recrystallization and globularization), the recrystallized phase constituents at least partially inherited the orientation of the coarse β -grains and colonies of α -lamellas in as-cast condition.

Thus, in the initial condition, the majority of the α -phase particles have rather homogeneous orientation, except some fragments (subgrains or cells)—compare the areas marked by the rectangles in Fig. 11a, c. Subsequent tension, in addition to the above-described changes in the microstructure in the zone of intense plastic flow (Figs. 10a, b, 12a), caused crucial changes in the local crystallographic orientations

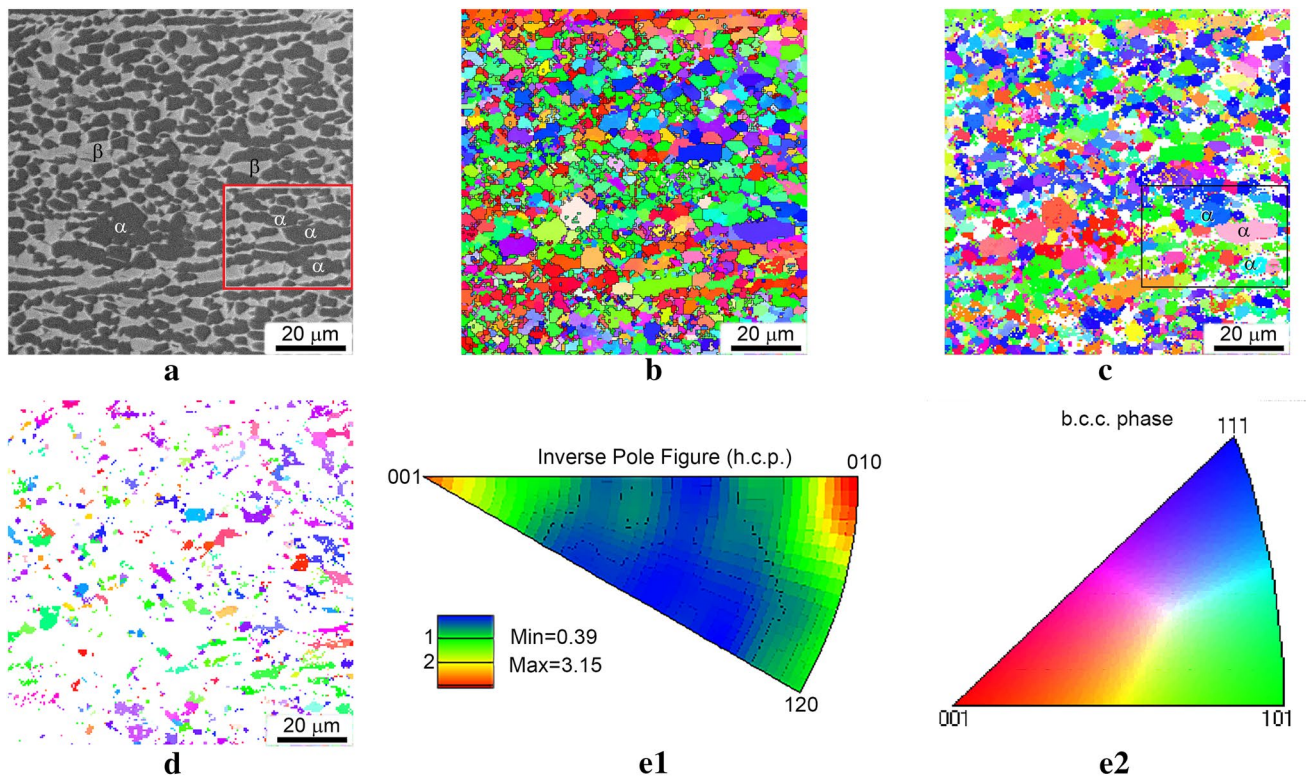


Fig. 11. (a) SEM BSE image of the annealed T110 sample cut out of 15 mm thick plate; (b) corresponding EBSD OIM of the α - and β -phase related to rolling direction (RD); (c) EBSD OIM of the α -phase related to normal direction (ND); (d) EBSD OIM of the

β -phase related to normal direction (ND); (e1) represents the inverse pole figure for h.c.p. α -phase; (e2) represents the inverse pole figure for b.c.c. β -phase.

(first of all for α -phase crystallites, Fig. 12b, c). As seen from Fig. 11b, c (initial state) and Fig. 12b, c (deformed material), there are zones with different crystallographic orientations inside *almost all* α -particles elongated in the tension direction (Figs. 12a vs. 11a). The size of these zones is almost an order of magnitude smaller than that of the particles in the initial condition before deformation (Figs. 12b, c and 11b, c). Since the size of the α -particles has changed insignificantly (except for a certain elongation), the evolution of the pole figures is supposedly a consequence of the formation of a developed cellular substructure with high (up to a few degrees) misorientation between adjacent subgrains. In other words, the EBSD studies of the annealed and then deformed T110 specimens revealed essential defragmentation of the primary α -phase particles near the fracture surface, with less noticeable changes in the boundaries of these particles—i.e., the α -phase particles with similar orientation consist of noticeably misoriented cells (fragments) formed during intense plastic flow. In turn, the β -phase has not undergone significant changes in orientation (compare Figs. 12d with 11d).

Changes in the internal crystallographic orientation of the subgrains formed inside the α -phase particles upon

tension are clearly seen in Fig. 13 where the misorientation angles between adjacent α -particles in the initial annealed state and after tension (A and B, respectively) are shown. Plastic deformation significantly increased the amount of high-angle boundaries inside the initial α -particles.

In the STA-hardened material, it was only possible to determine the orientation of the residual primary α_I -phase particles, whereas the $\alpha_{II} + \beta$ matrix around them was not indexed because of too fine dimensions of the α_{II} -needles and β -interlayers between them (not more than tens of nanometers in cross-section—see Fig. 3g). Upon the tension these remnants of α_I -phase formed parallel stripes of approximately the same crystallographic orientation like in as-annealed state (Fig. 14a, b, where $\alpha_{II} + \beta$ matrix is shown in light grey color). TEM studies of the microstructure in the zone near to the fracture surface revealed highly deformed state with enhanced density of dislocations and tweens in the remnants of primary α_I -particles. The substructure of the $\alpha_{II} + \beta$ matrix was difficult to discern (Fig. 14d). Nevertheless, taking into account that STA-hardened material demonstrated rather poor plastic flow due to hard ($\alpha + \beta$) matrix, it can be assumed that the

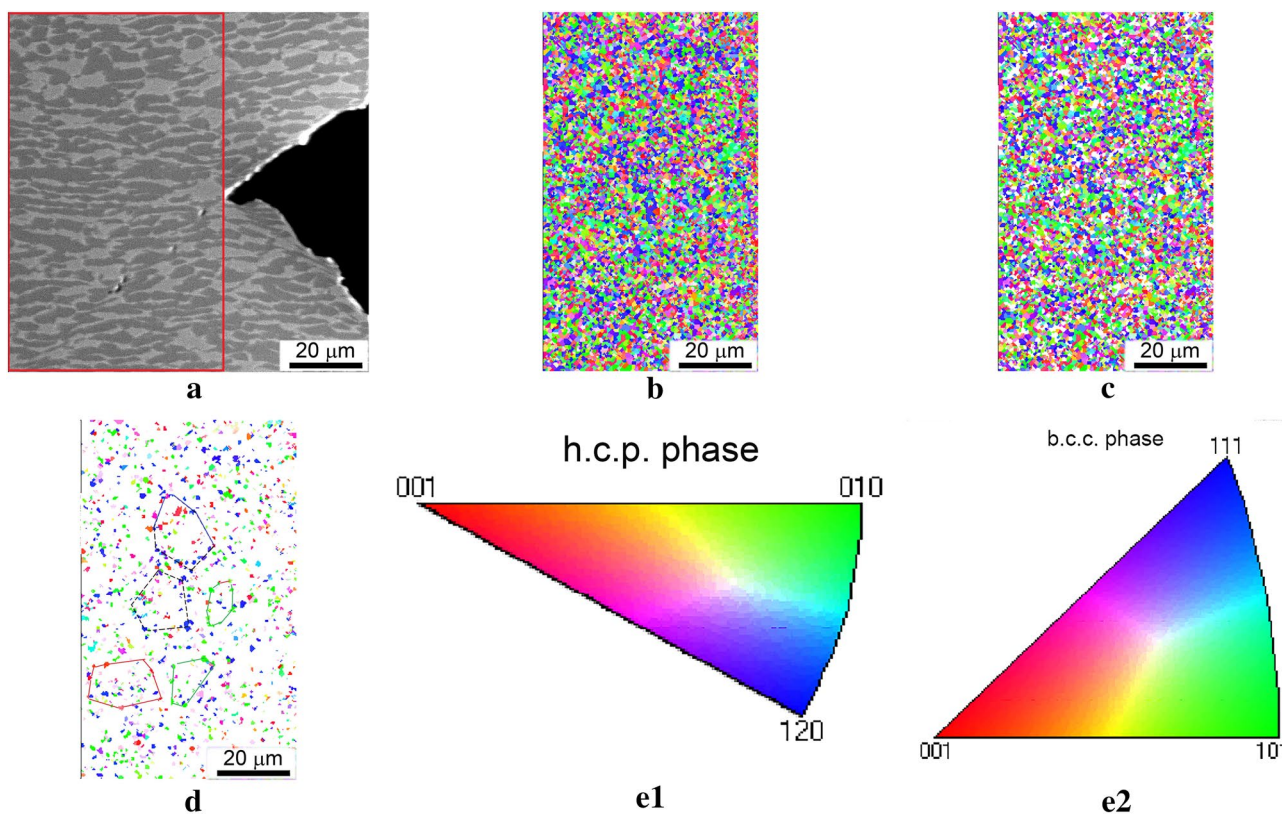


Fig. 12. The T110 material cut out from annealed 15 mm thick plate after tension with a rate of $8 \cdot 10^{-4} \text{ s}^{-1}$ near to the fracture surface: (a) SEM BSE image; (b) EBSD OIM of the α - and β -phase related to rolling direction (RD) close to the fracture surface indicated by the

rectangular in (a); (c) EBSD OIM of the α -phase; (d) EBSD OIM of the β -phase; (e1) represents the inverse pole figure for h.c.p. α -phase; (e2) represents the inverse pole figure for b.c.c. β -phase.

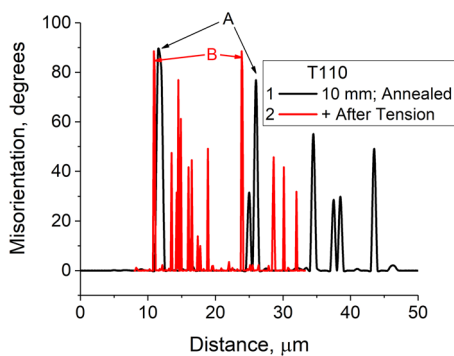


Fig. 13. Misorientation between adjacent α -particles in the specimens cut out from 10 mm thick plate of the T110 alloy in as-annealed condition (the view field is shown in Fig. 11a) and after tensile test (the view field is shown in Fig. 12a). “A” and “B” mark initial and deformed conditions, respectively.

deformation mainly localized inside the α_1 -globules, that caused their fragmentation into misoriented subgrains.

Microstructure Features of Specimens After Compression

Quasi-static Compression Typical examples of the microstructure of the T110 specimens after QSC tests are shown in Figs. 15, 16 and 17 for all studied annealed and STA-hardened materials. The microstructure of the specimens cut out from 15 mm thick plate in as-annealed condition and QSC-tested along the rolling direction (i.e., compressed in longitudinal direction) changed in the zones indicated in Fig. 1c in different ways (Fig. 15a–e). In the top layer near the contact surface between specimen and input bar (zone “A” in Fig. 15a), the microstructure changed insignificantly in comparison with initial state (compare Figs. 15b with 3b, c). More noticeable changes were observed in the top corner (Fig. 15c—zone “B” in Fig. 15a) and in bottom zone (Fig. 15d, zone “A₁” in Fig. 15a), where the main crack started and ended, respectively. It is quite obvious that in these zones, especially in “B,” the localized stresses from the zones “A” and “C” superimposed that led to a complex-stressed (both in magnitude and directions) state. As a result, in these zones, the particles of the α - and β -phases distorted their form and rotated. The relatively narrow bands

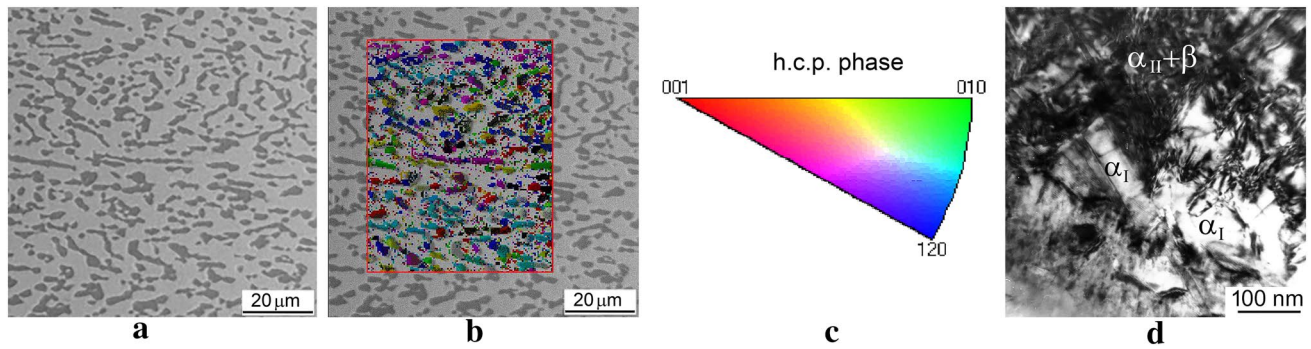


Fig. 14. (a) SEM BSE, (b) SEM+EBSD OIM of α -phase, (c) represents the inverse pole figure for h.c.p. α -phase and (d) TEM of the T100 alloy (15 mm thick plate) in STA-hardened state after tension with a strain rate of $8 \cdot 10^{-4} \text{ s}^{-1}$. TEM foil was taken from the zone shown in (a).

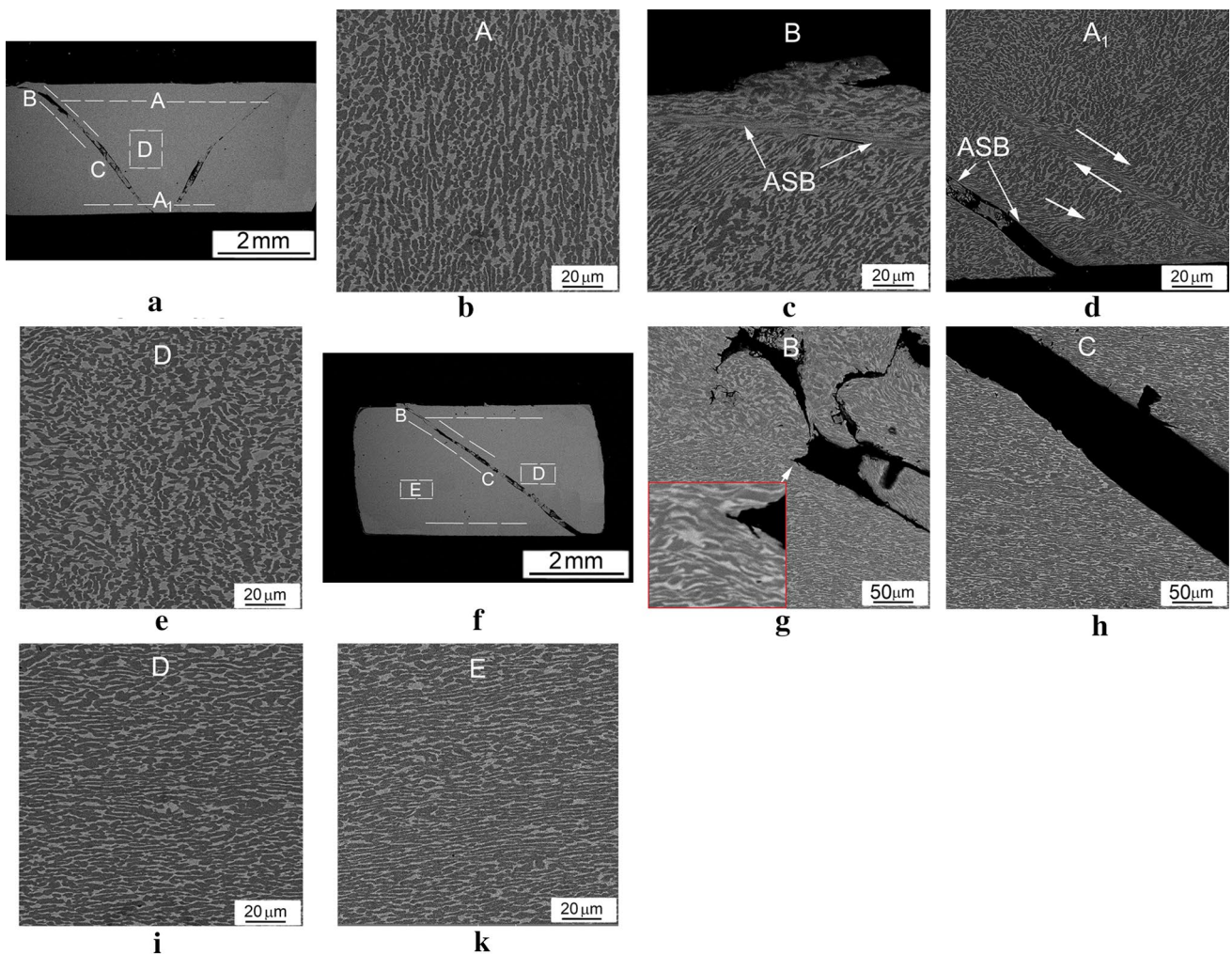


Fig. 15. Microstructure of the T110 specimens cut out from annealed 15 mm thick plate and QSC tested in the cutting directions: (a–e) RD and (f–k) TD. The letters in (b–e) and (g–k) indicate the loca-

tions marked in (a) and (f), respectively, and correspond to the zones shown in Fig. 1c. Compression was performed along vertical axis. SEM, BSE.

of localized plastic deformation (up to ASB appearance), some of which were parallel to the main crack (Fig. 15d),

were observed. In the central zone, a specific microstructure

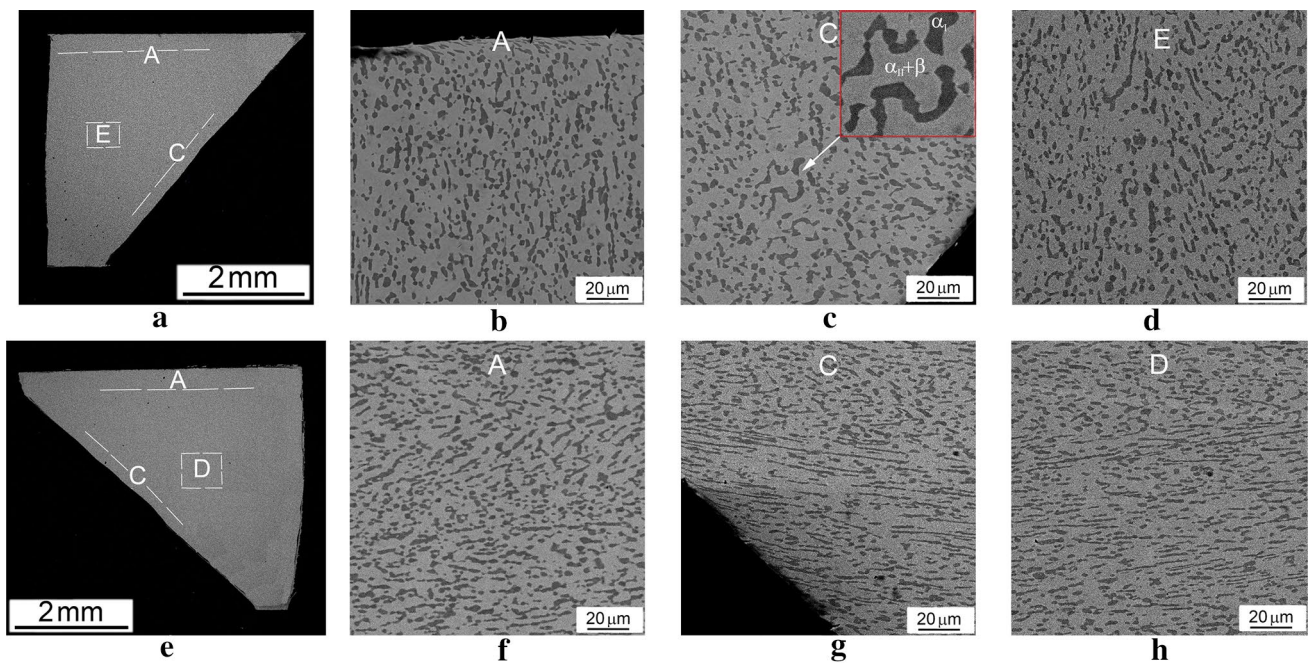


Fig. 16. Microstructure of the STA-hardened T110 material (15 mm thick plate) after QSC in the cutting directions: (a–d) RD; (e–h) TD. The letters in (b–d) and (f–h) indicate the locations marked in (a) and

(e), respectively, and correspond to the zones shown in Fig. 1c. Compression was performed along vertical axis. SEM, BSE.

with turned and fragmented particles of both phases was detected (Fig. 15e).

Microstructures of different types were identified in the annealed specimens tested by QSC method in transverse direction (Fig. 15f–k). The most intense deformation also occurred in the zone “B” due to the multidirectional forces action (Fig. 15g). Compressed layers of more flattened and stretched parallel to RD direction particles of α - and β -phases were observed away from the main crack (“D” and “E” in Fig. 15i, k, respectively), whereas in the areas close to the main crack the phase constituents were curved along the direction of crack propagation (Fig. 15h).

In the STA-hardened T110 material (Fig. 16a), compression along rolling direction caused visible changes in the shape and orientation of primary α_1 -particles in different locations (Fig. 16b–d), which were more evident close to the main crack surface (Fig. 16c) and specimen top (Fig. 16d), than in its center (Fig. 16b). In the corner of the sample (zone “B”), no microstructural changes different from those observed in the zone “A” were found out. Presumably, this was due to the fact that the hardened specimen cracked relatively earlier compared to more ductile annealed specimens. In turn, in the case of compression in the transverse direction, the changes in the microstructure were observed mainly near the crack (zone “C”; compare Fig. 16e–h). The fact that the α_1 -phase in the STA-hardened state had fewer signs of plastic deformation is a consequence of the presence of a

hardened $\alpha_{II}+\beta$ -matrix (Fig. 3d–g) that reduced the material plasticity by more than two times (compare Fig. 6a, b).

The microstructure of the T110 specimen cut out from annealed 10 mm thick plate and QSC tested is shown in Fig. 17. In general, the features of deformed microstructure are rather similar to those described above for the specimens cut out from 15 mm thick plate. Evident signs of plastic deformation were observed in the thin surface zone “A” (Fig. 17b). More intense deformation occurred in the corners of specimen (zone “B,” Fig. 17c) and along the main crack (zone “C,” Fig. 17d). Besides, the evidences of intense deformation were observed in the zone of secondary cracking (zone “D,” Fig. 17e). However, it should be taken into account that the specimen in this metallurgical condition had the highest plasticity and underwent maximum deformation under applied loading (Fig. 6c). In addition, no ASBs were observed, and the regions of localized plastic flow were much narrower than in the annealed specimens cut out from 15 mm thick plates (e.g., compare Figs. 15d and 17c or d).

The same material had somewhat lower plasticity when tested by QSC method in the transverse direction. It underwent earlier fracture (Fig. 6c), so the microstructural changes were less pronounced compared to the tests along the rolling direction (Fig. 17f–k). It is worthwhile to note that the maximum deformations were observed along the main crack in the zone “C₁” (Fig. 17i). In other locations, for example “C” and “D,” visible signs of deformation were observed in the form of fragmentation of separate relatively long (not

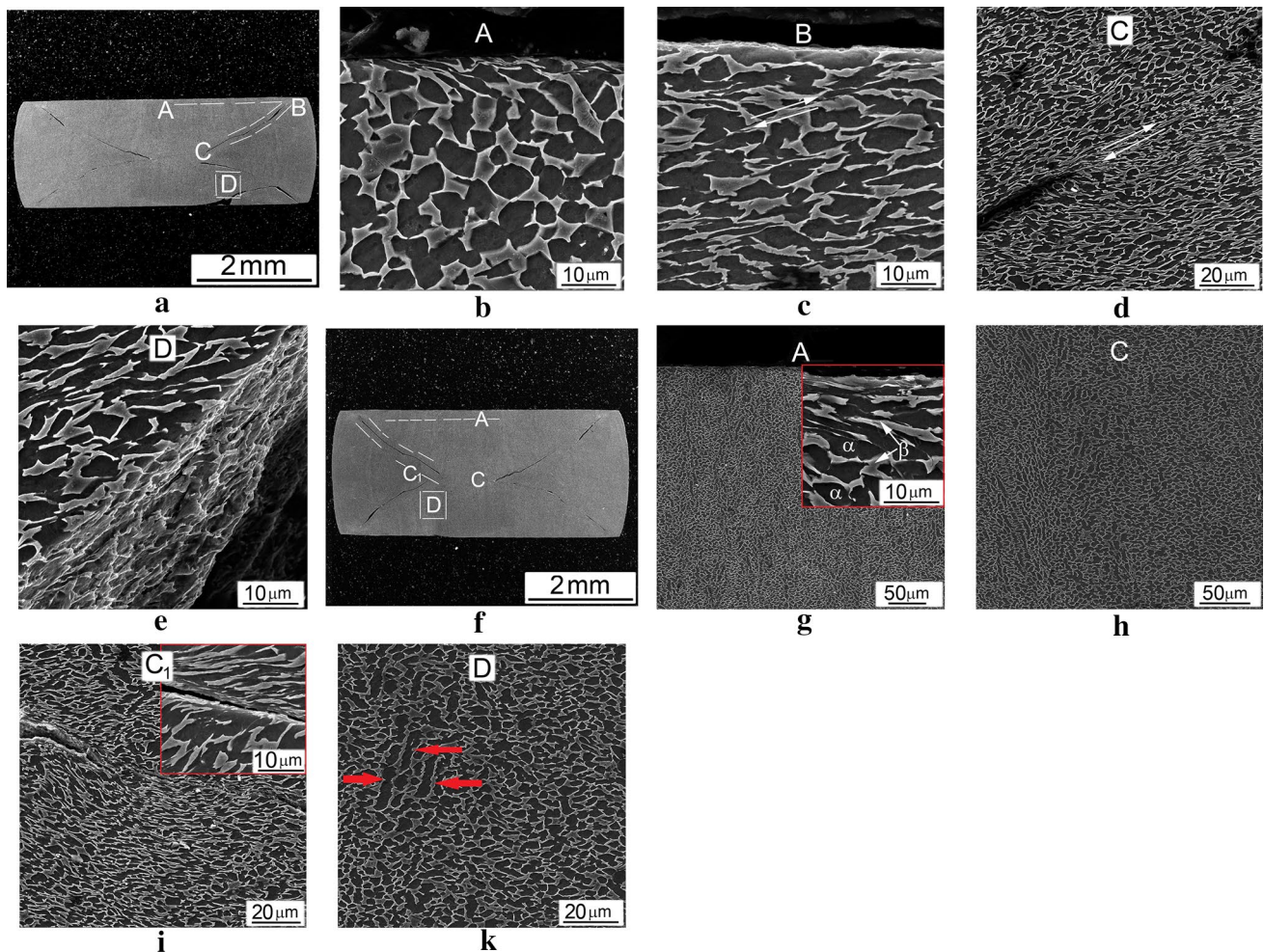


Fig. 17. Microstructure of specimens cut out of the annealed T110 10 mm thick plate after QSC tested for cutting directions: (a–e) RD; (f–k) TD. The letters in (b–d) and (f–h) indicate the locations marked

in (a) and (e), respectively. Arrows in (k) indicate unrecrystallized α -lamellas fragmented by deformation. Compression was performed along vertical axis. SEM, SEI.

globularized during annealing) α -particles (marked with arrows in Fig. 17k).

Comparison of QSC-tested specimens cut out of 15 mm (Fig. 15) and of 10 mm (Fig. 17) thick plates allows to conclude that the latter material was more ductile and cracked in the very last stages of deformation (e.g., compare Figs. 17f, 15f). There were no fundamental differences in the microstructure features between the specimens tested along (RD) and across (TD) rolling direction; the difference was only in the deformation level—it was higher in RD.

Thus, all the above results allow to conclude that the mechanical behavior of the T110 alloy under quasi-static compression, as well as tension conditions is determined by the peculiarities of the plastic flow of an ensemble of the α - and β -phases. The largest reserve of plasticity and the maximum values of strain energy are achieved when the morphology of the α -phase (the main phase constituent in the equilibrium state) is close to the equiaxial globular one,

and microstructure and crystallographic texture of alloy are close to isotropic in the macroscopic scale. Such material can be easily deformed by the simultaneous plastic flow of both α - and β -phases in the direction of applying the acting stresses. After reaching the stage of localization (necking under tension, and inside zones "B" and "C" under compression), pores nucleate inside of tested material, which cracks then. Compression tests are also characterized by the formation of bands of intense flow (up to the formation of ASB) at the stage before voids nucleation and cracking development. After thermal hardening, the alloy contained fine α_{II} -particles that caused significant strengthening, which in turn led to high localization of stresses at the interfaces between the hardened $\alpha_{II} + \beta$ -matrix and more ductile remnants of α_I -particles. As a result, the plasticity of the alloy significantly reduced, and the reserve of strain energy also dropped down.

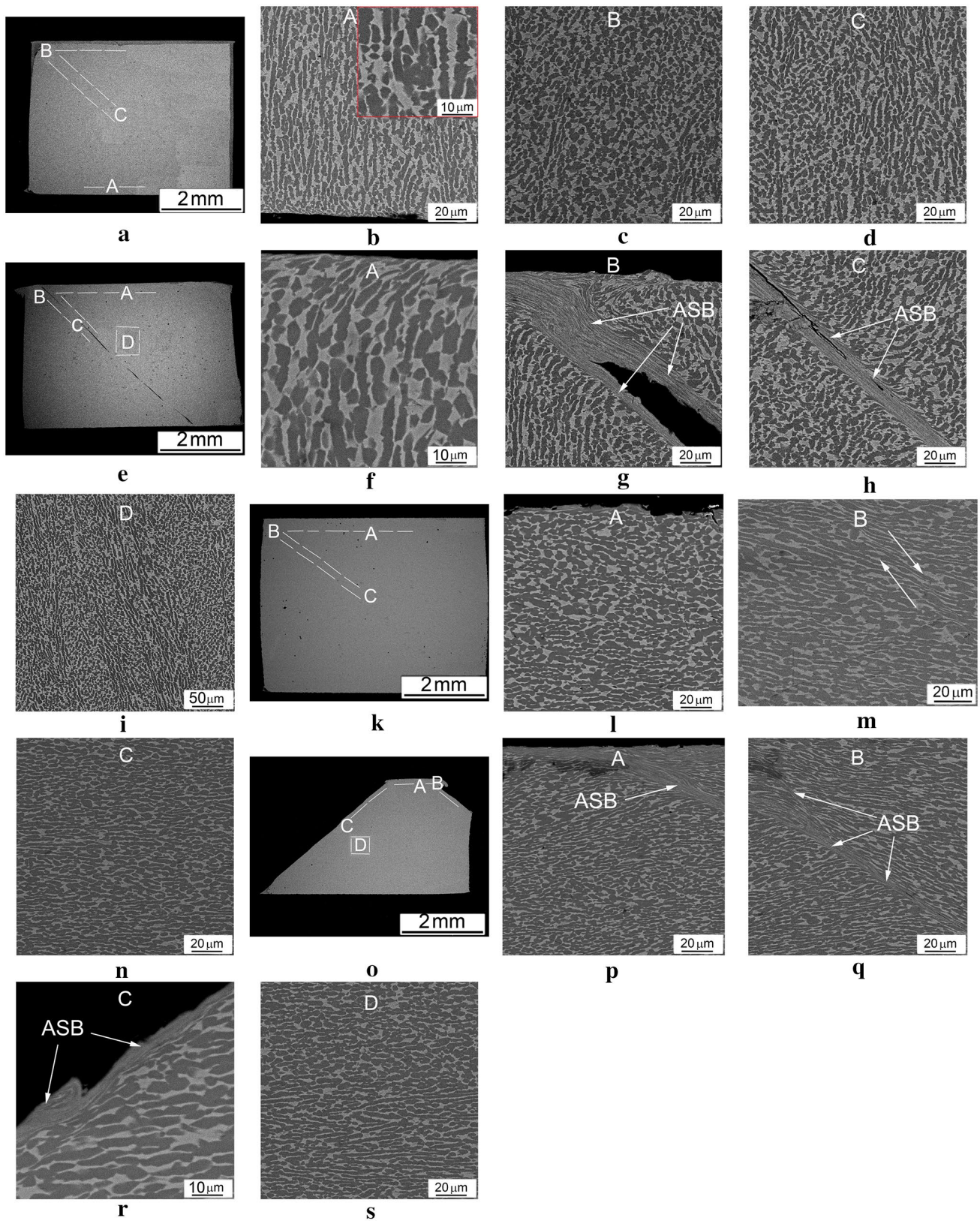


Fig. 18. Microstructure of the T110 material cut out from the annealed 15 mm thick plate tested under SHPB loading condition with strain rates (a–d) 2710 s^{-1} , (e–i) 3520 s^{-1} , (k–n) 2570 s^{-1} , (o–s)

2970 s^{-1} in (a–i) longitudinal and (k–s) transverse cutting directions. Specimens were loaded along vertical direction. SEM, BSE.

High-Strain Rate SHPB Tests 15 mm Thick Plate The microstructure features of the dynamically tested T110 are significantly affected, among other factors, by the rate of deformation, i.e., higher strain rates cause earlier fracture. At the strain rates below critical value $\dot{\epsilon}_{Cr}$, the most evident microstructural change in the annealed specimens tested in RD cutting direction (Fig. 18a) was the fragmentation of elongated α_1 -particles into chains of finer particles (Fig. 18b). Similar behavior was observed in various parts of the specimens, that was caused by complex stress state of different magnitude and direction have acted (Fig. 18c, d). The changes in orientation (slight rotation) of separate α_1 -particles were observed mainly in the edges of the specimens, which were subjected to more complicated stresses (zone “B” in Fig. 18b). At higher strain rates (when the specimens fractured—Fig. 18e–i), apart from local intensive distortion of α -particles in the narrow near-surface zone (zone “A” in Fig. 18f), ASBs appeared also in zones the “B” and “C,” inside which cracks nucleated (Fig. 18g, h, respectively). Moreover, the microstructure changes similar to those locally observed at lower strain rates (fragmentation and distortion of the primary α_1 -phase), appeared in various zones of the specimen tested at higher rates (Fig. 18f–i).

In the case of the transverse cutting direction specimens, in contrast to both high-strain rate tests and QSC tests in the longitudinal cutting direction, the main evidences of plastic deformation (Fig. 18k–s) appeared predominantly as the fragmentation of elongated plates/chains of the α -phase particles at all strain rates (Fig. 18l, n). It should also be emphasized the formation of localized shear bands at lower strain rates compared to the specimen compression in the rolling direction in zone “B” (Fig. 18m). At higher strain rates, the specimens fractured (Fig. 18o), and the ASBs and related cracks formed in various zones (Fig. 18p–r), except “D” (Fig. 18s). Evidently, these areas of highly localized deformation were initiated in the zone “B” and then crossed the sample along the zone “C” at an angle of 45° in accordance with Schmid’s law. Already at short distances from these zones of localized deformation, there were no visible traces of plastic deformation, unlike QSC tests (compare Fig. 18l, m, p, and especially 18s with Fig. 15k). Thus, the high-strain rate deformation is characterized by much higher localization of plastic flow in comparison to the quasi-static compression, possibly due to the lack of time for relaxation/redistribution of applied stresses.

It should be also underlined that the difference between SHPB behavior of the specimens loaded in RD and TD directions consisted in earlier cracking the TD specimens, i.e., at lower strain rates. It can be explained by earlier development of above-described features of the microstructure and crystallographic texture of the material loaded in the TD direction.

In the case of the STA-hardened T110 material tested at the SHPB conditions (Fig. 19a, e, i, n), the noticeable signs of plastic deformation were observed exclusively on the contact surface with the SHPB bars or close to it (input bar; the zones “A” and “B” in Fig. 19b, f, k, l, o), or near the main crack itself (Fig. 19g, p, q). In other locations, the microstructure looked practically unchanged (compare Figs. 19d, h, m with 3e). As at quasi-static tests, both for tension (Figs. 10c, 14a) and compression (Fig. 16), the remnants of the primary α_1 -phase in the areas far from the above-mentioned locations remained practically unchanged during high-strain rate deformation. Therefore, it can be concluded that in the thermally hardened condition, in contrast to the annealed one, the plastic flow is restricted by the $\alpha_{II} + \beta$ matrix, which has very low plasticity. Like in the annealed condition with essentially higher plasticity, the hardened T110 alloy fractured at much lower strain rates when tested in TD (1220 s^{-1}) as compared to RD (2430 s^{-1}) direction.

10 mm Thick Plate Typical examples of the microstructure of the specimens cut out from 10 mm thick plate in annealed condition after high-rate strain SHPB tests are shown in Fig. 20. The main microstructural changes are quite similar to those observed after the same tests of the specimens cut out from annealed 15 mm thick plate. It mainly concerns the localization of plastic deformation in the zones “A” and “B” with the highest local stresses (Fig. 20b, c). In the latter case (zone “B”), the bands of intense localized deformation similar to the ASBs were observed (Fig. 20c). In other locations, including the zone “C,” the signs of plastic deformation were less obvious, except some α -lamellas which were not transformed by recrystallization (Fig. 20b, d). Nevertheless, particles with typical martensite morphology were observed in the zone “E,” where the lowest stresses were acted (Fig. 20e). Local chemical analysis (Table 1) confirmed this observation and allowed to suggest that it was a joint result of the heating at high-strain rate compression and local depletion of the β -phase with β -stabilizing elements—compare the composition of the stable region of the β -phase (p. #2 in Table 1) with the transformed one (p. #1). This is in the good agreement with the well-known dependencies between the content of β -stabilizing elements and $\beta \rightarrow \alpha'(\alpha'')$ decomposition upon rapid cooling [23–25].

The specimens tested in TD direction (Fig. 20f–i) showed approximately similar changes of microstructure in the zone “A” like all others annealed T110 specimens tested at compression. The phase constituents were distorted by intensive plastic flow within very narrow (less than 10 micrometers) top layer (compare Figs. 20g with 17b and g, 18f, 19f, and 20b). As with other specimens, a shift of neighboring areas at an angle of about 45° was observed in the zone “B” (Fig. 20h); a “flattening” of the α - and β -phase particles in the middle part of the specimen (zone “C”) was observed (Fig. 20i).

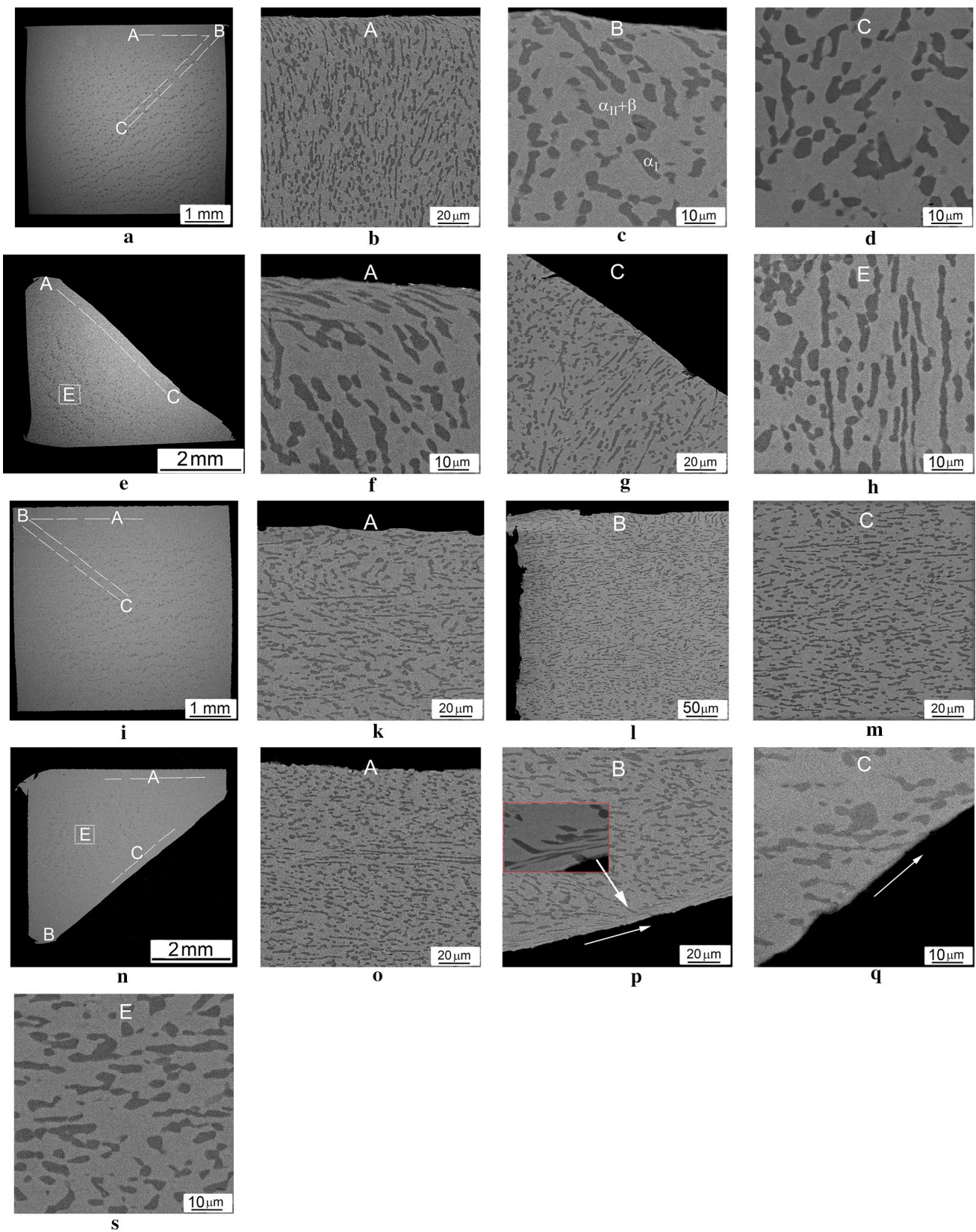


Fig. 19. Microstructure of the STA-hardened T110 specimens cut out from 15 mm thick plate tested under SHPB loading condition with strain rates (a–d) 1240 s^{-1} , (e–h) 2430 s^{-1} , (i–m) 1170 s^{-1} , (n–s)

1220 s^{-1} tested in directions: (a–h) RD, (i–s) TD. Specimens were loaded in vertical direction. SEM, BSE.

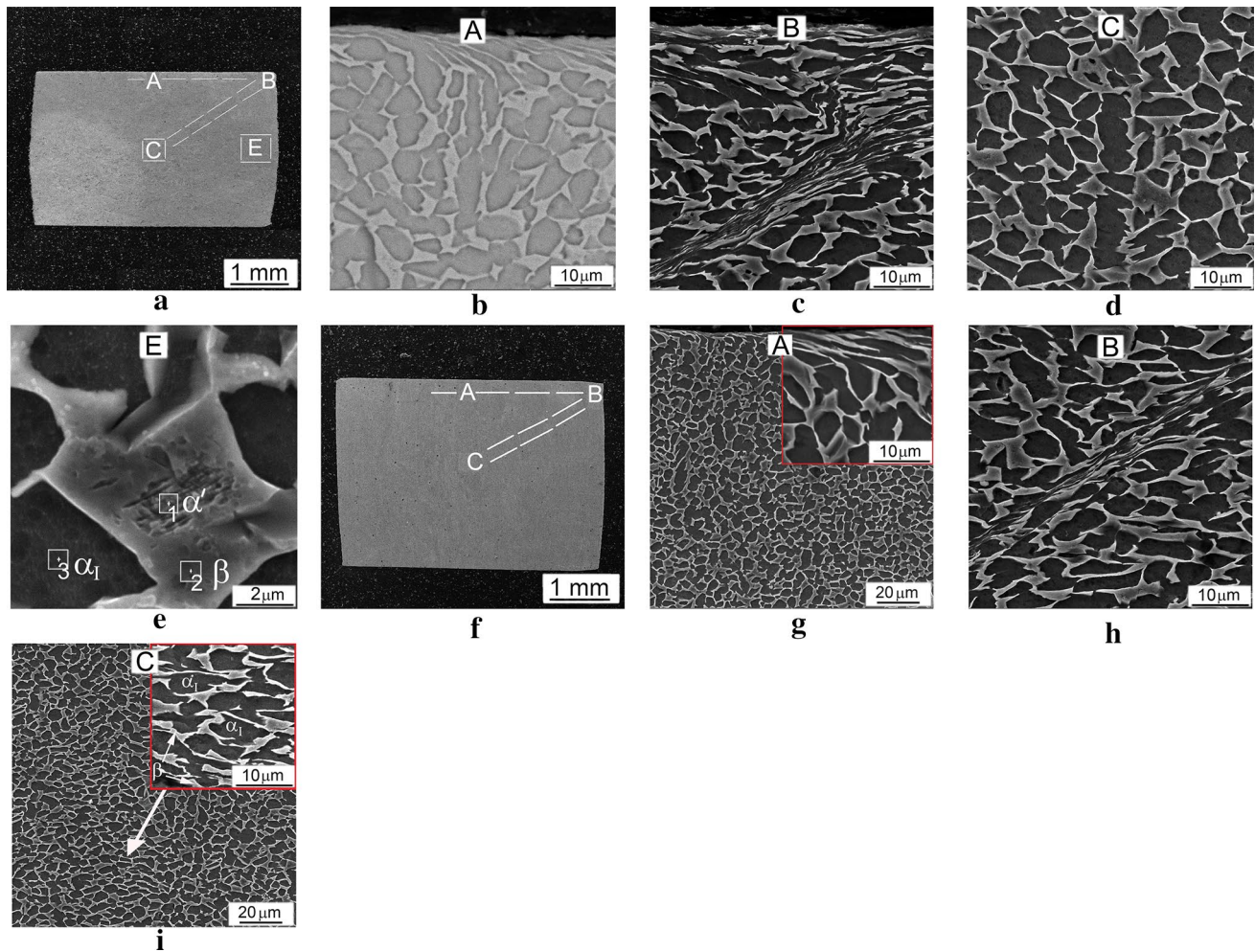


Fig. 20. Microstructure of specimens cut out from the annealed T110 10 mm thick plate tested under SHPB loading condition with strain rates (a–e) 2810 s^{-1} , 2200 s^{-1} in (a–e) RD, and (f–i) TD directions. Specimens were tested in vertical direction. SEM, (a, c–i) SEI, (b) BSE.

Table 1. Comparison of the chemical composition of the T110 alloy in areas marked in Fig. 20e with average content of alloying elements

| Point # | Chemical elements, wt.% | | | | | | | |
|---------------------|-------------------------|------|------|------|------|------|------|---------|
| | Al | V | Cr | Fe | Zr | Nb | Mo | Ti |
| 1 | 2.61 | 0.67 | 0.04 | 5.14 | 0.78 | 4.48 | 1.44 | Balance |
| 2 | 2.23 | 0.82 | 0.11 | 5.46 | 0.65 | 5.44 | 2.42 | |
| 3 | 4.83 | 0.00 | 0.06 | 0.40 | 0.39 | 1.83 | 0.43 | |
| Average composition | | | | | | | | |
| | 3.90 | 0.8 | 0.14 | 2.10 | 0.70 | 3.80 | 1.50 | Balance |

Several attempts to obtain EBSD data after QSC or high-strain rate SHPB tests were mostly unsuccessful due to significant residual stresses and high density of defects present in the specimens after intense deformation. One of most representative results obtained on an annealed specimen compressed in the rolling direction with a rate of 2810 s^{-1} is shown in Fig. 21. As can be seen, the high-rate deformation resulted in the fragmentation of the majority of initial

α -phase particles into subgrains (compare Figs. 21b with 11b).

The main difference in comparison to quasi-static compression consists in that with the increase in strain rate the time for stress distribution over the sample volume and relaxation decreases multiple times, resulting in more and more localization of the deformation. Dynamic course of deformation also causes an intensive increase in localized temperature by adiabatic heating, which, in turn, has

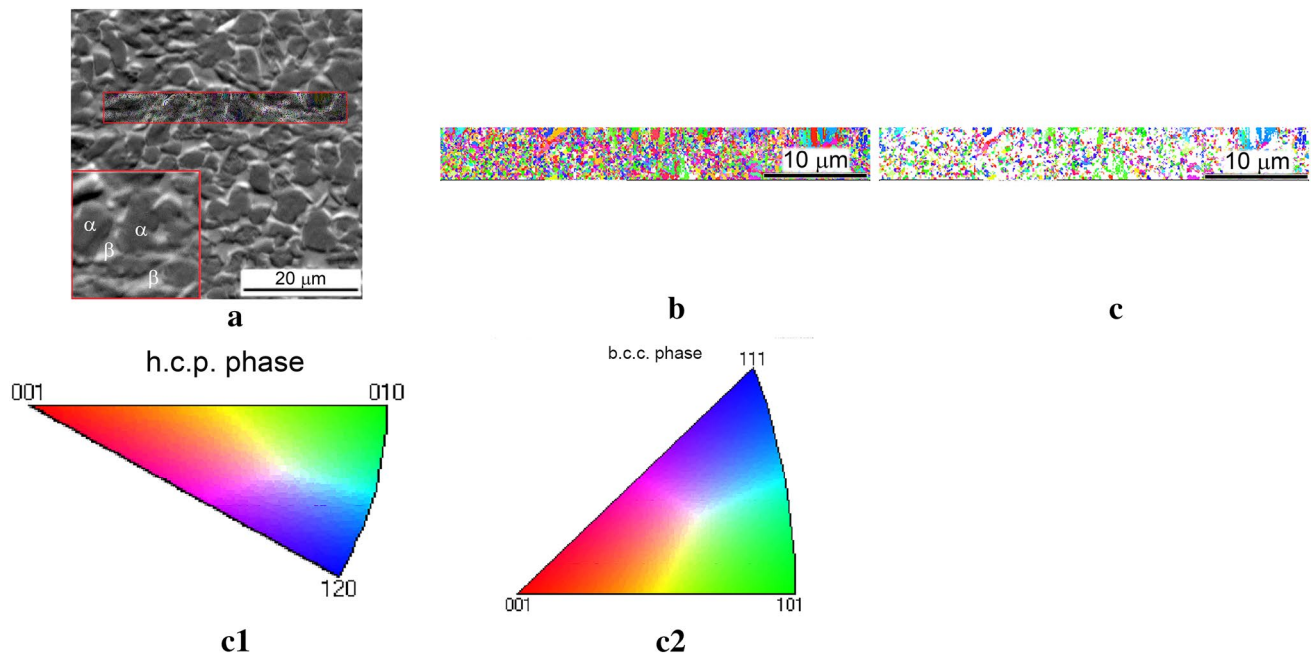


Fig. 21. The T110 specimen cut out from annealed 10 mm thick plate after high-strain rate (2810 s^{-1}) SHPB test in RD: (a) SEM BSE (zone “C” shown in Fig. 20d) with superposed OIM; (b, c) EBSD

OIMs of (b) both α - and β -phase; (c) β -phase; (c1) represents the inverse pole figure for h.c.p. α -phase; (c2) represents the inverse pole figure for b.c.c. β -phase.

a significant effect on deformation processes in these local volumes due to material softening.

Generalizing obtained data, it should be underlined that the T110 is a very promising titanium alloy—in well-processed condition it has a uniform and relatively fine globular microstructure that ensures a good balance of mechanical properties on tension and compression in a wide range of strain rates. These T110 alloy properties are higher than the wide-spread Ti-6Al-4V alloy in the same microstructural state. This explains the previously established fact that plates of different thickness made of the T110 alloy showed essentially better terminal ballistic resistance than the plates of similar thickness made of Ti-6Al-4V. It makes possible to replace the latter alloy with the T110 alloy in the most responsible parts, for which price [26] is not a limiting factor.

It is obvious that the improved balance of mechanical properties of the T110 alloy in comparison with Ti-6Al-4V is provided due to its more complex alloying system. The same approach was applied, for example, in the development of new titanium high-strength weldable alloys and welding wire. Due to the content of various β -stabilizing elements, it ensured their mutual substitution in the weld metal, which in turn provided their sufficient uniform total distribution [7, 8, 27–29]. Similar cooperative effect of alloying elements was observed in the multi-component titanium alloys during phase transformations (upon interphase movement [30]), and during homogenization of high-temperature β -phase [31]

under non-equilibrium conditions upon continuous high-rate heating. Higher content of β -stabilizing elements expressed in terms of molybdenum equivalent [32] in the T110 ($C_{Mo} \geq 4.5 \text{ mas. \%}$ vs. $\approx 3 \text{ mas. \%}$ for Ti-6Al-4V) caused in higher amount of β -phase in annealed condition—approximately up to 20% (see Fig. 3c, h) vs. 7% in Ti-6-4 [1]. Due to this tensile strength of the annealed T110 exceeds 1100 MPa (Fig. 5a, c), while for the best annealed state of Ti-6Al-4V, it is not more than 950 MPa at approximately the same ductile characteristics [1]. It is this combination of strength and ductility in quasi-static tests that ensures the superiority of T110 over Ti-6Al-4V in terms of strain energy (see Fig. 8ab, b).

Additionally, the special role of niobium in titanium alloys should be mentioned. Being relatively “weak” β -phase stabilizer [23, 33, 34], niobium has a particularly beneficial effect on the plasticity of titanium alloys [35, 36]. The effect of niobium can be explained by the peculiarities of its interaction with the atoms of titanium matrix from the viewpoint of electron structure [37, 38].

Conclusions

The features of the mechanical behavior of the new thermally hardenable medium-level alloyed two-phase α + β titanium alloy T110 under conditions of quasi-static tension and compression loading conditions, as well as high-strain rate

compression, were studied for several initial microstructural states. It was established the following:

1. The approach based on the determination of strain energy parameter allowed to compare both annealed and thermally hardened states in terms of their resistance to an applied external load.
2. It is established that the annealed state with a more uniform microstructure of globular morphology has essentially better balance of strength and ductility in all types of tests carried out. Good balance of mechanical properties is explained by both the uniformity of the phase structure and crystallographic texture.
3. Application of conventional solution treatment, water quenching, and final aging strengthening led to a significant increase in strength, but drastically decreased plasticity of the alloy. As a result, the strain energy parameter in the annealed states was essentially higher, especially for quasi-static tests.
4. The morphological texture in the form of remnants of incompletely recrystallized lamellas of the α -phase and grains of the β -phase elongated along the rolling plane has a greater effect on the mechanical behavior, especially in dynamic tests, than the crystallographic texture of even the hexagonal close-packed α -phase. In this sense, a more globularized annealed state formed at a higher degree of deformation at the temperatures of the two-phase field ($\epsilon_{\text{total}} = 3$) has a noticeable superiority over the less perfect one ($\epsilon_{\text{total}} = 2$). Under high-strain rate loading, the increased plasticity reserve provided by the globular microstructure is more important from the viewpoint of the overall durability/reliability of titanium alloys, than the strength achieved by hardening heat treatment.
5. Detailed study of microstructure and local crystallographic texture (EBSD method) allowed to find out some specific features of deformation mechanisms. Upon quasi-static tension of the alloy in the annealed state, the zones of localized intense plastic deformation in the region of neck formation were observed, where the α - and β -phase particles were pulled out in the direction of tension stresses. In the necking zone voids were formed, followed by cracking at the α/β interphase boundaries. In the thermally hardened state material, due to the high strength of the $\alpha_{\text{II}}+\beta$ matrix, voids formed exactly at the boundaries between this matrix and the remnants of the primary α_1 -phase at earlier stages of plastic deformation. During compression, deformation occurred in different ways in various zones, depending on the magnitude and direction of local stresses. The highest stresses, and hence the maximum plastic deformation, were observed in the zone crossing the sample at an angle of 45° , as well as in the corners of the sample, where the zone intersected with the surface layer severely deformed under contact with input and output bars of the SHPB system. The annealed and hardened state materials differed in the same way as in tension, i.e., the main deformations were localized at the boundaries between the $\alpha_{\text{II}}+\beta$ matrix and the remnants of the primary α_1 -phase. The main difference between quasi-static and dynamic compression tests was that with increase in strain rate increase the time for stress distribution over the specimen volume and relaxation decreased, that resulted in higher and higher localization of deformation. Besides, the local adiabatic heating under high-strain rate compression played additional role in deformation processes.
6. Comparison with the data previously obtained for the Ti-6Al-4V alloy with similar microstructure and tested at the similar test conditions shows that the T110 with well-processed uniform globular microstructure is evidently superior in the case of quasi-static tests and demonstrates almost the same high-strain rate mechanical response under compression.

Acknowledgements This research received no special funding. Present studies were performed according the Agreement of Cooperation between G.V. Kurdyumov Institute for Metal Physics of N.A.S. of Ukraine and Jarosław Dąbrowski Military University of Technology, Poland. Some separate works in G.V. Kurdyumov Institute for Metal Physics were financed by N.A.S. of Ukraine within the frames of the research project #III-09-18.

The authors would like to thank M.A. Skoryk (G.V. Kurdyumov Institute for Metal Physics of N.A.S. of Ukraine) for help in performing the EBSD study.

Declarations

Conflict of interest The authors declare no conflict of interest.

References

1. G. Luetjering, J.C. Williams, *Titanium*, 2nd edn (Springer, Berlin, 2007) <https://doi.org/10.1007/978-3-540-73036-1>
2. R.R. Boyer, R.D. Briggs, The Use of β Titanium Alloys in the Aerospace Industry. *J. Mater. Eng. Perform.* **14**, 681 (2005). <https://doi.org/10.1361/105994905X75448>
3. M. Niinomi, Recent metallic materials for biomedical applications. *Metall. Mater. Trans.* **33A**, 477 (2002)
4. J. Fanning, Military application for β titanium alloys. *J. Mater. Eng. Perform.* **14**, 686–690 (2005). <https://doi.org/10.1361/105994905X75457>
5. S.L. Semiatin, An overview of the thermomechanical processing of α/β titanium alloys: current status and future research opportunities. *Metall. Mater. Trans. A.* **51**, 2593–2625 (2020). <https://doi.org/10.1007/s11661-020-05625-3>
6. O.M. Ivasishin, D.G. Savvakina, O.O. Stasiuk, V.A. Golub, V.I. Mirnenko, S.G. Sedov, V.A. Kurban, S.L. Antonyuk, P.E. Markovsky, Microstructure and properties of titanium-based materials

- promising for antiballistic protection. *Progr. Phys. Met.* **20**(2), 288–309 (2019). <https://doi.org/10.15407/ufm.20.02.052>
7. V.M. Zamkov, V.P. Topol'sky, M.P. Trigub, et al., Patent of Ukraine #40087, 16.06.2003.
 8. Ye.V. Abolil'hina, S.L. Antinyuk, O.G. Molyar, V.M. Zamkov, Fatigue fracture of welded specimens made of T110 alloy. *Mater. Sci.* **40**, 535–538 (2004). <https://doi.org/10.1007/s11003-005-0073-2>
 9. P. E. Markovskiy, V.I. Bondarchuk, S.V. Akhonin, A.V. Berezos, Electron beam cold hearth melted titanium alloys and the possibility of their use as anti-ballistic materials, in *Proceedings of 14th World Conference on Ti, 10–15 June, 2019, Nantes, France, MATEC Web of Conferences*, vol. **321**, p. 11036 (2020). <https://doi.org/10.1051/mateconf/202032111036>.
 10. O.M. Ivasishin, S.V. Akhonin, D.G. Savvakina, V.A. Berezos, V.I. Bondarchuk, O.O. Stusyuk, P.E. Markovskiy, Effect of Microstructure, Deformation Mode and Rate on Mechanical Behavior of Electron-Beam Melted Ti-6Al-4V and Ti-1.5Al-6.8Mo-4.5Fe Alloys, *Progress in Physics of Metals*, 2018, 19(3), pp. 309–336. Doi: <https://doi.org/10.15407/ufm.19.03.309>
 11. <http://spctitan.pwi-scientists.com/eng>
 12. S.V. Akhonin, F.N., Pikulin, V.A. Berezos, et. al., Laboratory electron beam unit UE-208M, (in Russian), *Sovremennaya elektrometallurgiya*, 2019, #3, pp. 15–22. <https://doi.org/10.15407/sem2019.03.03>
 13. Chen W.; Song B. Split Hopkinson (Kolsky) Bar: Design, Testing and Applications, Springer, Berlin, 2011. <https://doi.org/10.1007/978-1-4419-7982-7>
 14. H. Kolsky, Propagation of stress waves in viscoelastic solids. *Appl. Mech. Rev.* **11**, 465–468 (1958)
 15. H. Kolsky, Stress waves in solids. *J. Sound Vib.* **1**, 88–110 (1964). [https://doi.org/10.1016/0022-460X\(64\)90008-2](https://doi.org/10.1016/0022-460X(64)90008-2)
 16. P.E. Markovskiy, J. Janiszewski, V.I. Bondarchuk, O.O. Stasyuk, M.A. Skoryk, D.G. Savvakina, K. Cieplak, P. Dziewit, S.V. Prikhodko, Effect of strain rate on microstructure evolution and mechanical behavior of titanium based materials. *Metals*. **10**(11), 1404 (2020). <https://doi.org/10.3390/met10111404>
 17. R.R. Boyer, *Titanium and its alloys: metallurgy, heat treatments and alloys characteristics, encyclopedia of aerospace engineering* (Wiley, New York, 2010) <https://doi.org/10.1002/9780470686652.eae198>
 18. P.E. Markovskiy, V.I. Bondarchuk, Influence of strain rate, microstructure, chemical and phase composition on mechanical behavior of different titanium alloys. *J. Mater. Eng. Perform.* **26**(7), 3431–3449 (2017). <https://doi.org/10.1007/s11665-017-2781-9>
 19. P.E. Markovskiy, V.I. Bondarchuk, O.M. Herasymchuk, Influence of grain size, aging conditions and tension rate on mechanical behavior of titanium low-cost metastable beta-alloy in thermally hardened condition. *Mater. Sci. Eng. A* **645**, 150–162 (2015). <https://doi.org/10.1016/j.msea.2015.08.009>
 20. P.E. Markovskiy, Mechanical behavior of titanium alloys under different conditions of loading, material science. *Forum*. **941**, 839–844 (2018)
 21. R.W.K. Honeycomb, *The Plastic Deformation of Metals* (Edward Arnold Publication Ltd, London, 1984) <https://doi.org/10.1002/crat.2170200506>
 22. G. Lutjering, Influence of processing on microstructure and mechanical properties of ($\alpha + \beta$) titanium alloys. *Mater. Sci. Eng. A*. **243**, 32–45 (1998). [https://doi.org/10.1016/S0921-5093\(97\)00778-8](https://doi.org/10.1016/S0921-5093(97)00778-8)
 23. Y.C. Huang, S. Suzuki, H. Kaneko, T. Sato, Continuous cooling—transformation of β -phase in binary titanium alloys, in *The Science, Technology and Application of Titanium* (Oxford: Pergamon Press, 1966), pp. 695–698.
 24. W. Zhang, W.S. Zhao, D.X. Li, M.L. Sui, Martensitic transformation from α -Ti to β -Ti on rapid heating. *Appl. Phys. Lett.* **84**(24), 4872–4874 (2004). <https://doi.org/10.1063/1.1762698>
 25. M. Bignon, E. Bertrand, P.E.J. Rivera-Díaz-del-Castillo, F. Tancrét, Martensite formation in titanium alloys: crystallographic and compositional effects. *J. Alloy. Compd.* **872**, 159636 (2021). <https://doi.org/10.1016/j.jallcom.2021.159636>
 26. <https://www.titanium-alloy.com/>.
 27. V.N. Zamkov, S.L. Antonyuk, A.G. Molyar, New high-strength weldable titanium alloy T110, in *Metallic Materials with High Structural Efficiency* (eds.: O.N. Senkov et.al), 2004, Kluwer Academic Publication, pp. 269–278.
 28. A.A. Babaréko, I.V. Égiz, M.A. Khorev, Effect of supplementary alloying of titanium alloy VT23 on its phase composition and tendency to recrystallization. *Met. Sci. Heat Treat.* **35**, 116–120 (1993). <https://doi.org/10.1007/BF00773810>
 29. A.I. Khorev, High-strength titanium alloy VT23 and its applications in advanced welded and brazed structures. *Weld. Int.* **24**(4), 276–281 (2010). <https://doi.org/10.1080/09507110903319925>
 30. O.M. Ivasishin, H.M. Flower, The redistribution of alloying elements by rapid heat treatment of an $\alpha + \beta$ titanium alloy. *J. Mater. Sci.* **21**, 2519–2524 (1986). <https://doi.org/10.1007/BF01114300>
 31. V.I. Bondarchuk, P.E. Markovskiy, Features of multicomponent diffusion of alloying elements in titanium metastable β -alloys on continuous rapid heating. *Metallography. Adv. Technol.* **42**(9), 1217–1230 (2020). <https://doi.org/10.15407/mfint.42.09.1217>
 32. P. J. Bania, Beta titanium alloys and their role in the titanium industry, in *Beta Titanium Alloys in the 90's* (TMS Publications, Warrendale, PA, USA, 1993), pp. 3–14.
 33. F. Duwez, The martensite transformation temperature in titanium binary alloys. *Trans. ASM.* **45**(6), 934–940 (1953)
 34. L. Zhang, L. Xu, S. Xiao, Y. Chen, Effect of Nb addition on microstructure, mechanical properties and castability of β -type Ti–Mo alloys. *Trans. Non-Ferrous Soc. China.* **25**(7), 2214–2220 (2015). [https://doi.org/10.1016/S1003-6326\(15\)63834-1](https://doi.org/10.1016/S1003-6326(15)63834-1)
 35. Y. Guo, K. Georarakis, Y. Yokoyama et al., On the mechanical properties of TiNb based alloys. *J. Alloys Compd.* **571**, 25–30 (2013). <https://doi.org/10.1016/j.jallcom.2013.03.192>
 36. Y.-H. Hon, J.-Y. Wang, Y.-N. Pan, Composition/phase structure and properties of titanium-niobium alloys. *Mater. Trans. Jpn. Inst. Met.* **44**(11), 2384–2390 (2003)
 37. M. Abdel-Hady, K. Hinoshita, M. Morinaga, General approach to phase stability and elastic properties of b-type Ti-alloys using electronic parameters. *Scr. Mater.* **55**(5), 477–480 (2006). <https://doi.org/10.1016/j.scriptamat.2006.04.022>
 38. A.N. Timoshevskii, S.O. Yablonovskii, O.M. Ivasishin, First-principles calculations atomic structure and elastic properties of Ti-Nb alloys. *Funct. Mater.* **19**(2), 266–271 (2012)

Publisher's Note Springer Nature remains neutral with regard to jurisdictional claims in published maps and institutional affiliations.